# Dual-Functional Green Facile synthesis of graphene doped CuO-SnO2:F sprayed thin film as an efficient photocatalyst and ammonia gas sensor at low concentration

Ghofrane Charrada, Mejda Ajili, Sandrine Bernardini, Khalifa Aguir, Najoua Turki Kamoun

# Dual-Functional Green Facile synthesis of graphene doped CuO-$SnO_2$:F sprayed thin film as an efficient photocatalyst and ammonia gas sensor at low concentration.

Ghofrane Charrada [a, b] *, Mejda Ajili [a], Sandrine Bernardini [b],Khalifa Aguir [b] and Najoua Turki Kamoun [a]

(a)Université de Tunis El Manar, Faculté des Sciences de Tunis, Département de Physique, LR99ES13 Laboratoire de Physique de La Matière Condensée (LPMC), 2092, Tunis, Tunisia

(b)Aix-Marseille Université, Université de Toulon, CNRS IM2NP (UMR 7334), FS St Jérôme S152, Marseille, 13397, France

***e-mail : ghofrane.2019.charrada@gmail.com**



## Abstract

Undoped and graphene-doped CuO-$SnO_2$:F thin films were synthesized using spray pyrolysis technique with varying graphene ratios (Gr/(Gr + Cu)) of 2%, 4%, and 6%. These thin films were thoroughly characterized using X-ray diffraction (XRD), Scanning Electron Microscopy (SEM), Transmission Electron Microscopy (TEM), UV-Vis-NIR spectrophotometry, and impedance spectroscopy. Their performance was evaluated for photocatalytic degradation of various pollutants, including Green Malachite (GM), Rhodamine B (RdhB) and Methylene Blue (MB) dyes under sunlight irradiation, as well as for gas sensing of ammonia ($NH_3$) in the concentration range of 5–25 ppm at 250°C.

The photocatalytic activity was significantly enhanced in the case of the 6% graphene-doped CuO-$SnO_2$:F thin film. This improvement is attributed to the substantial reduction in the bandgap energy, from 3.092 eV to 2.238 eV for $SnO_2$:F and from 1.500 eV to 1.450 eV for CuO, upon graphene doping. These bandgaps narrowing facilitate to improve absorption of sunlight, resulting in higher photocatalytic efficiency. Similarly, the 6% graphene-doped CuO-$SnO_2$:F sensor demonstrated superior gas sensing performance, which can be explained by the

increase of the porosity and conductivity introduced by graphene. These changes promote efficient charge transfer and improve the adsorption of ammonia molecules on the sensor's surface, leading to higher sensitivity and faster response and recovery times.

Based on the advantages indicated above and the benefits of its simple structure, cost-effective fabrication, and the inherent advantages of the p-type semiconductor properties, the 6% graphene-doped CuO-$SnO_2$:F thin film presents a promising dual-functional material. It offers a high photocatalytic performance for pollutants degradation under sunlight and an excellent gas sensing capability for detecting low concentrations of ammonia (5-25 ppm), making them highly suitable for environmental and industrial applications.

**Keywords:** p-type CuO-$SnO_2$:F thin films, graphene doping effect, physical properties, ammonia gas sensing, environmental applications, spray pyrolysis.

## 1. Introduction

Air and water pollution are two of the most pressing environmental challenges of our time, posing serious threats to ecosystems, human health, and biodiversity. These forms of pollution disrupt natural cycles and contribute to global crises [1-3].

Water pollution arises from contaminants like plastic waste, industrial discharge, and agricultural runoff, severely harming aquatic ecosystems and limiting access to clean drinking water. This pollution threatens marine life and human health, prompting the scientific community to seek effective, sustainable solutions [4-5]. Among the most promising approaches for water pollution mitigation is solar-powered photocatalysis using metal oxide thin films [6]. These materials, known for their chemical stability and ability to degrade organic pollutants, offer a low-cost and eco-friendly method to combat water contamination [7].

However, challenges remain, as many metal oxide semiconductors can only absorb ultraviolet light, restricting their industrial applicability and flexibility [8].

To address the difficulty of activating metal oxides in the visible spectrum, extensive research efforts have focused on narrowing their band gaps. One effective strategy has been doping, which introduces impurities into the metal oxide structure to alter its electronic properties and enhance its performance. Upadhyay et al., in their pioneering work, highlighted the potential of graphene-doped metal oxide composites, including CuO, $SnO_2$, $TiO_2$, and ZnO, in advancing water treatment technologies [9].

Graphene, a two-dimensional carbon-based material with exceptional electrical, thermal, and mechanical properties, plays a multifaceted role in these composites. Firstly, graphene acts as a corrosion inhibitor, preventing the degradation of metal oxides and ensuring their long-term stability in aqueous environments [10]. Secondly, it limits the dissolution of metal oxide nanoparticles into the water, which is crucial for minimizing environmental and health risks associated with nanoparticle contamination [11].

Furthermore, graphene significantly improves photocatalytic efficiency by mitigating the electron-hole recombination process, which is a major limitation in traditional photocatalysts [12-15].

By serving as an electron acceptor, graphene facilitates the separation of photo-induced charge carriers increases the lifetime of reactive species, such as hydroxyl radicals and superoxide ions. These reactive species are essential for degrading pollutants and breaking down organic contaminants in water [16].

The synergistic interaction between graphene and metal oxides not only enhances photocatalytic activity under visible light but also broadens the application scope of these materials in sustainable water purification systems [17].

Similarly, The emission of harmful gases in the atmosphere, especially ammonia ($NH_3$), has significantly increased over recent decades due to intensive human activities such as over-fertilization in agriculture, food processing, and emissions from automobiles Ammonia exposure poses serious health risks, including irritation of the eyes, nose and throat, respiratory issues and in severe cases lung damage [18]. Given these dangers, the development of highly efficient gas-sensing devices capable of detecting $NH_3$ even at low concentrations have shoved the researchers to enhance the sensing capabilities of metal oxide semiconductors. [19].

Metal oxide semiconductors (MOSCs) are widely studied for gas-sensing applications due to their sensitivity and tunable properties. However, the utilization of MOSCs for ammonia detection faces significant challenges, such as high $NH_3$ concentration thresholds required for detection, prolonged response and recovery times, and reduced performance in practical environments [20-24]. Notably, the World Health Organization (WHO) has set the exposure limit for ammonia concentration at 25 ppm, highlighting the need for sensors capable of operating reliably at trace levels [25].

Recent advancements have demonstrated that graphene-doped metal oxides are promising materials for gas-sensing applications, owing to graphene's exceptional physical and chemical properties [26]. Graphene can modify the electronic structure and surface properties of metal oxides enhances their interaction with gas molecules and improving detection capabilities [27]. In this context, Graphene doped $WO_3$ nanocomposite has been successfully elaborated by Salama et al [28]. The results show a better gas sensing performance for ammonia gas compared with Undoped $WO_3$ nanoparticles [28].

In this study, improved $NH_3$ gas sensing activities and photocatalytic performance have been demonstrated at the first time for graphene doped CuO-$SnO_2$: F thin films using spray pyrolysis technique, offers a low cost , green and stable material in the time [29, 30].

This work aims to detect ammonia gas at trace level concentrations and remove organic pollutants (Green Malachite (GM), Rhodamine B (RdhB) and Methylene Blue (MB)) from water using solar energy-driven photocatalysis technique based on graphene doped CuO-$SnO_2$:F mixed oxide thin films to preserve the environment for future generations.

## 2. Experimental details

Undoped and graphene doped CuO-$SnO_2$:F mixed oxide thin films were deposited on glass substrates by spray pyrolysis technique. All required chemical materials ($CuCl_2$, $SnCl_4$, Methanol) have been purchased from Sigma Aldrich with high purity(>99%) ensuring fabrication of good quality thin films.

Firstly, the glass substrates (2.5 × 2.5 cm) are cleaned in an ultrasonic bath for 15 min. Then we prepare two solutions of copper and tin oxides. The $SnO_2$:F solution (0.2 M) was prepared using 2.3 ml of $SnCl_4$, 0.7 ml of $H_2O$ and 97 ml of methanol as precursors . Fluorine doping is achieved by adding 0.12 g of ammonium fluoride ($NH_4F$) to the total spray solution of 100 ml following these chemical reactions [31]:

$$SnCl_4 + 2H_2O \rightarrow SnO_2 + 4HCl \quad (1)$$

$$O^{2-} + F \rightarrow O + F^- + e^- \quad (2)$$

The CuO solution (0.2 M) was made by dissolving 3.4 g of copper chloride dehydrate ($CuCl_2$) in 100 ml of de-ionized water pursuing this chemical reaction [32]:

$$CuCl_2 + H_2O \rightarrow CuO + 2HCl \quad (3)$$

After that, both solutions were mixed with a molar ratio ($[Cu]_{sol}/[Sn]_{sol}$) equal to 3 [32-35]. The two solutions were mixed thoroughly for 15 minutes to ensure complete homogenization and facilitate uniform interaction between the components, which is essential for consistent results in the subsequent process.

Graphene was added to the resulted solution as doping, with a ratio $\frac{[Gr]}{[Cu]+[Gr]}$ $0,2,4\ and\ 6\%$ .The spray nozzle is located at 27 cm above the substrate, the flow rate is maintained at 10 $ml.min^{-1}$ and the deposition temperature is fixed at 350°C for all samples during the experimental process [35]. The as-prepared thin films carried several characterizations such as X-ray diffraction measurement (XRD) using a diffractometer system equipped with Cu as an anode material with radiation Cu-Kα (λ= 1.5406 Å). The measured patterns were recorded in the scanning range of $10° < 2\theta < 80°$. Surface morphology was performed using Cari Zeiss GmbH T3447 scanning electron microscopy (SEM) and JEOL JEM-2010 Transmission Electron Microscopy (TEM), which facilitate the investigation of the morphology and crystallinity of the thin layers. In addition, optical properties were studied through aPerkin Elmer Lambda 950 spectrometer in the wavelength range from 250 to 1800 nm. Furthermore, Impedance measurements were operated by applying two electrodes on the film's edges using silver paste. The impedance data was collected employing E4980A analyzer with a frequency ranging from 2 KHz to 2 MHz at room temperature.

In photocatalytic process, the as-prepared samples were immerged in 40 ml of diverse aqueous solutions containing various pollutants (Green Malachite (GM), Rhodamine B (RhB) and Methylene Blue (MB)). The suspension was agitated for 30 min in dark before being exposed to sunlight, in order to achieve the maximum adsorption of our organic pollutants onto catalysts. The degradation process was controlled by an UV-VIS-NIR spectrophotometer.

To study the sensing performance of the homemade devices, all samples are annealed at 500°C in air during 2 hours. After that, electrodes, which are made from gold and chromium with thickness of 100 nm and 5 nm, respectively were deposited on undoped and graphene-doped CuO-$SnO_2$: F based sensors by magnetron sputtering method. Gold offers good stability at high temperatures, and chromium is used to enhance the adhesion of gold on the substrate [36-37].

The measurements were carried out in a closed test chamber using a Keithley 2450 Source Meter model data acquisition system.

## 3. Results and discussions

### 3.1 Structural properties

The material phases and crystallite properties of undoped and graphene doped CuO-$SnO_2$: F coupled oxide thin films elaborated at different doping levels were analyzed using X-ray diffraction (XRD) measurements in 2θ scanning range of 10° to 80°, as shown in Figure 1. The distinct diffraction peaks observed at 2θ = 26.21° and 38.33° corresponded to the crystal planes (110) and (200) of the tetragonal structure of $SnO_2$: F (JCPDS # 88-0287), respectively [32]. Additionally, a polycrystalline character related to the monoclinic structure of CuO was identified by the dominant peaks (110), (-111) and (020) located at 2θ = 33.1°, 35.2° and 51.8° respectively (JCPDS # 89-5895) [38]. The presence of both CuO and $SnO_2$: F phases confirm the successful synthesis of CuO-$SnO_2$: F coupled oxide thin films without any other secondary phases for all samples. At first glance, Graphene doped-CuO-$SnO_2$:F with different doping concentrations (2%, 4%, 6%) shown the absence of graphene peak in XRD patterns, which can be explained by two possible scenarios: the low amount of graphene or its high dispersion in the nanometer size range that is difficult to appear in XRD chart [39]. It is important to highlight that at a doping level equal to 6%, the preferred orientation was changed from (110) for both

CuO and $SnO_2$:F to (-111) for CuO and (200) for $SnO_2$:F accompanied by an increase in crystallinity (Fig.1).

The average crystallite size (D) was calculated based on the widening of the diffraction peaks using the Scherrer's relation [40]:

$$D = \frac{k\lambda}{\beta\cos(\theta)} \qquad (4)$$

Where k represents the Scherrer's constant (k=0.9), $\lambda$ is the wavelength of the X-ray beam (λ= 0.15406 nm), Θ is the Bragg angle and β is the full width at half maximum.

To delve deeper into the crystal structure of the material, we conducted calculations to determine dislocation density (δ) according to the following relation [41]:

$$\delta = \frac{1}{D^2} \qquad (5)$$

The crystallite size and dislocation density are reported in Table1. According to this table, we notice that the average size of the crystallites increases by increasing graphene concentration. The maximum crystallite size (21 nm) is observed for the 6% graphene-doped thin film, which gives a minimum value of dislocation density equal to 2.27 x $\mathbf{10}^{-3}$nm$^{-2}$ . As a bi-dimensional material graphene can act as a nucleation site for the growth of larger grains [42-43].

In gas sensing, the improve of stability by reducing the number of defects helps to maintain consistent sensor performance over time. Similarly, for catalysis, making them advantageous for long-term and efficient catalytic processes [44].

### 3.2 Morphological study

The morphological images of undoped (Fig.2.a) and 6% graphene-doped CuO-$SnO_2$:F samples (Fig.2.b) were collected by SEM analysis at different magnifications (1μm and 300 nm) are presented in figure 2. The results reveal different morphologies, including nano-cubic structure corresponding to CuO , and nano-sphere structure corresponding to $SnO_2$ [45] (Fig.2.c and Fig.2.d). After doping with graphene, we observed the formation of additional voids. This change in morphology is beneficial for catalytic and gas sensing applications [46]. The increase of voids and porosity create more surface area and expose more active sites, which are critical for enhancing interactions with target gases. The presence of graphene, with its high aspect ratio and exceptional mechanical strength, likely contributes to these morphological changes, facilitating the formation of voids and improving the adsorption capacity [47]. This type of microstructure is advantageous for gas detection and photocatalytic applications, as it promotes better sensitivity and efficiency in detecting and interacting with gases [48-49].

The TEM spectra of undoped and 6% graphene-doped CuO-$SnO_2$:F thin films (Fig.2.e and Fig.2.f) provide valuable insights into the structural and morphological characteristics of the composite material [50]. The analysis reveals that, with increasing graphene doping, a noticeable increase in the crystallite size was observed, which is in accordance with XRD results [51]. This growth in crystallite size suggests improved crystallinity and structural ordering, which is advantageous for enhancing the stability and electronic properties of the thin films. These structural modifications are highly beneficial for applications in gas sensors and catalysis [52].

### 3.3 Optical properties

The knowledge of the optical properties of materials holds great significance in the design and analysis of optoelectronic devices. The optical transmission T (λ) and reflection R (λ) spectra of undoped and graphene doped CuO-$SnO_2$: F coupled oxide thin films elaborated at different doping levels in the wavelength range of 250–1800 nm are shown in Fig.3 ((a) and (b)). In the wavelength of 250-1800 nm, the transmission intensities of all samples exhibit a low transparency coefficient between 20% and 45 % in the visible range [300-900] nm and increased sharply to reach 66 – 75 % in the NIR (Fig.3 (a)). The transmission is found to be maximal for the undoped CuO-$SnO_2$: F thin films and it decreases with an increase in graphene (Gr) content. This may be attributed to the increase in surface charge due to the presence of Gr. Furthermore, Strong absorptions were observed in the wavelength region of 800-900 and below 600 nm which correspond to the band gap of the individual CuO and $SnO_2$ phases, respectively [53]. The reflection spectra of the undoped and graphene doped CuO-$SnO_2$: F thin films at different doping levels is depicted in (Fig.3 (b)). The behavior of reflection as a function of wavelength is the same for all synthesized films and the average reflectance is less than 20 % in the visible range.

As a means to evaluate the band gap energy (Eg) of all synthesized films, we used two methods. First, the Tauc formula which involves plotting the relationship between the absorption coefficient (α) and the photon energy (hν), and then extrapolating the linear portion of the $(\alpha h\nu)^2$ curve to the x-axis (photon energy) intercept as depicted in Fig.4. The point where the extrapolated line intersects the x-axis represents the optical band gap energy of the thin film material [54]:

$$\alpha h\nu = A\,(h\nu - E_g)^n \qquad (6)$$

Where A is a constant related to the material, h is Planck's constant; n corresponds to ½ for direct transitions and 2 for indirect transitions, and α was calculated using this equation [55]:

$$\alpha = \frac{1}{e}\ln\frac{(1-R)^2}{T} \qquad (7)$$

Where e is the film thickness. Second, $E_g$ was evaluated by the differential of the Transmission spectra of the layers for undoped and Gr-doped (2%, 4% and 6%) CuO-$SnO_2$:F thin films. In Fig.5 (a, b, c and d) are presented the dT/dλ versus wavelength for undoped and Gr-doped (2%, 4% and 6%) CuO-$SnO_2$:F thin films. This method is used to confirm the band gap values. From Table 2, it is evident that both Tauc and Differentiate methods yield approximately the same band gap values, which strongly validates the accuracy and reliability of the obtained values [56].

The presence of two distinct band gaps for our samples indicates the coexistence of two phases, CuO and $SnO_2$, which is correlated with XRD spectra. The Undoped CuO-$SnO_2$: F thin films revealed two band gaps of 1.501 eV for CuO phase and 3.092 eV related to $SnO_2$ material. The obtained band gaps have different values than that reported for CuO (1.2 eV) and $SnO_2$ (3.8 eV) [57]. These differences indicated the charge transfer may be occurred between CuO and $SnO_2$ films, leading to a modification in the electronic structure of both oxides, which ultimately changed the band gap values. Fig.6 displays the effect of Gr content on the band gap of CuO and $SnO_2$ phases. Insertion of 2 wt% Gr decreased the band gap of $SnO_2$ from 3.092 to 2.743 eV. In addition, further decrease was observed for CuO and $SnO_2$ band gaps with increasing the concentration of Gr from 2 to 6 wt% (Table 2). These values shift from 1.500 to 1.450 eV and from 2.743 to 2.238 eV, respectively for CuO and $SnO_2$:F. Several factors influence the band gap of metal oxides such as defects, carrier concentrations, impurities, disorder at the grain boundaries and particles. In the case of Graphene doping material, the reduction in the band gap can be attributed to its electronic structure (good electron acceptor) in CuO [58] and donor in $SnO_2$:F [59]. That can affect the width of the localized regions of conduction and valence band with the formation of various optically active sub-levels through the band gap, resulting

in a decrease in its optical band gap [60]. In fact, Gr reduces the energy band gap by removing of Burstein–Moss effect and it causes transition of the absorption edge of the $SnO_2$ toward higher wavelengths [61]. According to this approach, the band gap of $SnO_2$ semiconductor is moving towards a lower energy with increasing electron density in the conduction band [62].

From the reflection-transmission spectra R (λ) and T (λ), we have calculated different optical parameters characterizing these thin layers such as the refractive index (n) and the extinction coefficient (k). The complex refractive index is calculated using the following formula [63]:

$$\mathbf{n^* = n + ik} \qquad \textbf{(8)}$$

The real part (n) describes the ratio of the speed of light in a vacuum compared to its value in the material. The imaginary part (k) represents the extinction coefficient, this describes how much the light is absorbed or attenuated as it passes through the material. Both real and imaginary components are calculated by applying the following equations, which are derived from the fundamental properties of light interacting with matter [64]:

$$\boldsymbol{k = \frac{\alpha\lambda}{4\pi}} \qquad \textbf{(9)}$$

$$\mathbf{n = \frac{1+[1-(\frac{1-R}{1+R})^2(1+k^2)]^{1/2}}{(\frac{1-R}{1+R})}} \qquad \textbf{(10)}$$

The refractive index (n) increases from 1.66 for undoped CuO-$SnO_2$: F to 2.15 for 6% Gr-doped CuO-$SnO_2$: F as shown in Fig.7 (a). On the other hand, the value of k decreases with increasing wavelength from ultraviolet (UV) to visible region, after it increases slightly in the near infrared (NIR) region (Fig.7 (b)).

The changes in both n and k, depending on graphene doping level and wavelength demonstrate the versatility of CuO-$SnO_2$: F thin films and their potential for various optoelectronic applications.

A high refractive index in materials can offer significant advantages for gas sensing and catalytic applications. In gas sensors, materials having a high refractive index can enhance light-matter interactions, leading to improve sensitivity and selectivity in detecting gases [65]. This is especially important for detecting trace amounts of gases like ammonia, where enhanced optical properties can improve the sensor's ability by increasing gas adsorption. In catalysis, a high refractive index material can facilitate better light absorption and scattering, promoting more efficient photocatalytic processes. It can help in concentrating light energy at the catalytic surface, enhancing reaction rates and overall catalytic performance [66]. Therefore, materials with a high refractive index are beneficial for both gas sensing and catalytic applications by improving detection sensitivity and promoting more efficient chemical reactions [67].

**3.4 Impedance spectroscopy**

The impedance spectroscopy is a powerful analytical technique widely used in materials science to investigate the electrical properties of materials and their interfaces. By applying an alternating current (AC) signal over a range of frequencies, it enables the measurement of complex impedance, which provides insight into processes such as charge transport, polarization, and relaxation mechanisms within materials [68].

The complex impedance Z*(ω) is written as the following relation [69] :

$$Z^*(\omega) = Z'(\omega) - iZ''(\omega) \qquad (11)$$

where Z' (ω) and Z'' (ω) are respectively the real and imaginary parts of the complex impedance as a function of the frequency ω. Next, $Z'(\omega)$ is plotted on the x-axis and $Z''(\omega)$

on the y-axis to create a Nyquist plot, allowing for a deeper understanding of electrical parameters by using Z-View software. It is observed from that the impedance spectrum of all thin films represent a single semi-circle that indicates the Debye type of relaxation [70].

The equivalent circuit is composed of two Resistances R1, R2 and a Capacitance C1, as shown in Fig.8 (a). The impedance spectra of the as-prepared thin films were illustrated in Fig.8 ((b) and (c)).

The fitting values of the impedance measurements of all thin films obtained via Z-view software are summarized in Table 1. It was found that the introduction of graphene leads to the decrease of the semi-circle diameter (Fig.8.c), which means that the conductivity is enhanced by increasing the graphene doping level [71]. This phenomenon occurs due to several factors. Firstly, graphene, with its unique two-dimensional structure, serves as an excellent conductor due to its high electron mobility. When incorporated into the CuO-$SnO_2$:F matrix, graphene provides additional pathways for electron transport, reducing the resistance within the film. Moreover, the presence of graphene can modify the band structure of CuO-$SnO_2$:F thin films, leading to the creation of defect states that facilitate charge carrier movement. Additionally, graphene's high surface area-to-volume ratio promotes better contact between the internal Nano-junction, further improving conductivity by reducing interfacial resistance [72-74]. Overall, doping graphene into CuO-$SnO_2$: F thin films offer a synergistic approach to enhance conductivity, making them promising materials for various optoelectronic applications.

## 4. Environmental applications

### 4.1. Photocatalytic degradation of organic dyes

Methylene blue, green malachite, and rhodamine B are prominent contaminants frequently detected in water sources, stemming from industrial processes, agricultural runoff, and

domestic waste. These pollutants not only taint water quality but also pose serious threats to aquatic life and human health due to their toxic nature and potential carcinogenic effects [75-76]. Addressing their removal is imperative for environmental sustainability. Solar-powered Photocatalysis emerges as a promising strategy to degrade pollutants into harmless products. However, the efficiency of photocatalysis relies heavily on the choice of catalyst material [77]. Therefore, there is a pressing need to innovate and engineer novel materials with enhanced photocatalytic properties, which is the subject of this study.

Fig.9 ((a) ,(b) and (c)) depicts the photocatalytic efficacy of undoped and Graphene doped CuO-$SnO_2$:F mixed oxide thin films, after 2 hours of exposure to sunlight. It is evident that the characteristic absorption peaks of MB, GM, and RdhB at wavelengths of 670 nm, 612 nm, and 567 nm, respectively, exhibit a decrease in peak intensity related to the increase in graphene doping levels [78-79].

Concerning the reaction kinetics, the degradation reactions of organic pollutants through heterogeneous photocatalysis typically adheres to pseudo-first-order kinetics. This implies that the rate of change in pollutant concentration over time is primarily dependent on the concentration of the pollutant itself, following a first-order reaction rate equation [80]:

$$\ln\left(\frac{C}{C_0}\right) = -k_1 t \quad (12)$$

Where $k_1$ represents the first-order rate constant, while $C_0$ and C denote the initial and final concentrations of the dye, respectively.

Fig.10 ((a), (b) and (c)) illustrates the plot of ln ($C/C_0$) as a function of time. In these plots, all thin films demonstrate first-order pseudo rate behavior, indicating their efficiency in removing organic pollutants. The rate constants corresponding to each thin film are shown in Fig.11.

The photo-degradation efficiency of all pollutants are calculated using the following relation [81]:

$$\text{effecienty} = \frac{C_0 - C}{C_0} * 100 \qquad (13)$$

All results are illustrated in Table 3. It was found that 6% Gr doped CuO-$SnO_2$: F thin films has the highest efficiency compared to other prepared samples, with a value equal to 99%, 87% and 91% for MB, GM and RdhB respectively after two hours of sunlight irradiation. Figures 12 represent photo-degradation rates of various pollutants and at various irradiation time ((a) methylene blue (MB), (b) green malachite (GM) and (c) rhodamine B (RdhB)) using various catalysts (undoped and graphene doped CuO-$SnO_2$:F thin films at different graphene concentration).

The pollutant degradation mechanism of undoped and graphene-doped CuO-$SnO_2$: F coupled oxide thin films involve several steps.

Upon exposure to sunlight, the semiconductor absorbs photons, generating electron-hole pairs in both CuO and $SnO_2$:F thin layers. While CuO can absorb visible light due to its narrow band gap, $SnO_2$:F remains inactive due to its broader band gap (Eq.14) [82]. Subsequently, the photo generated electrons and holes migrate to the interface between the two semiconductors, where they are efficiently separated, and preventing recombination. This separation is vital for the degradation process's effectiveness (Eq.15) [83]. The photogenerated electrons in the conduction band of $SnO_2$:F and the holes in the valence band of CuO participate in redox reactions with adsorbed pollutant molecules on the semiconductor surface, leading to their degradation into harmless products such as carbon dioxide. Reactive oxygen species, like hydroxyl radicals, are also generated during the process through reactions involving adsorbed oxygen and water molecules (Eq.16-17), playing a crucial role in organic pollutant degradation due to their high reactivity. Finally, the degradation of pollutants occurs through surface reactions facilitated by the active species generated on the semiconductor surface, including processes like the oxidation of organic compounds by reactive oxygen species or the direct interaction of pollutant molecules with photo generated charge carriers (Eq.18-19) [84-85].

$$CuO/SnO_2: F + h\nu \rightarrow CuO\ (e^- + h^+)\ /SnO_2: F \quad (14)$$

$$CuO\ (e^- + h^+)/SnO_2: F \rightarrow CuO\ (h^+)/SnO_2: F\ (e^-) \quad (15)$$

$$SnO_2: F\ (e-) + O_2 \rightarrow O_2^- + SnO_2:F \quad (16)$$

$$CuO\ (h^+) + H_2O \rightarrow h^+ + OH^- + CuO + \frac{1}{2}H_2 \quad (17)$$

$$O_2^- + \text{polluants} \rightarrow \text{Products} \quad (18)$$

$$h^+ + \text{polluants} \rightarrow \text{Products} \quad (19)$$

Graphene-doped CuO-$SnO_2$:F thin films involve the same mechanism of undoped CuO-$SnO_2$:F thin films [86]. However, the excellent dispersion of graphene nanoparticles within the material surface and the increase of porosity leads to more active sites available for catalytic reactions, which is correlated, with morphological results. Furthermore, Graphene doped CuO-$SnO_2$:F extend more in the visible range especially for 6% doping level (Fig.3(a)). For those reasons, Graphene doped CuO-$SnO_2$: F coupled oxide thin films show higher photocatalytic activity compared to undoped samples [87].

Finally, we have compared the efficiency of our synthesis of thin films with previous studies, which examined the degradation of pollutants such as methylene blue (MB), green malachite (GM), and rhodamine B (RdhB) (Table 4) [88-95]. Our composite material demonstrates superior performance, making it a promising candidate for various industrial applications. Its enhanced degradation efficiency signifies a potential breakthrough in addressing environmental challenges associated with pollutant removal.

### 4.2. Ammonia gas detection

Ammonia (NH3) gas is an hazardous substance commonly found in industrial emissions, agricultural activities, and various environmental sources. Exposure to high concentrations of

ammonia can lead to severe health issues such as respiratory irritation, lung damage, and even long-term chronic conditions [96]. Moreover, ammonia is a major contributor to air pollution, which can have detrimental effects on both human health and the environment, including the formation of fine particulate matter and acid rain. Due to its potential risks, there is an urgent need to develop high-performance sensors capable of detecting even trace amounts of ammonia gas [96]. Such sensors are crucial for ensuring safety in industrial settings, improving air quality monitoring, and protecting public health. Advances in sensor technology, particularly with materials like graphene-doped CuO-$SnO_2$:F thin films, hold great promise in addressing this challenge by providing sensitive, reliable, and cost-effective solutions for detecting low levels of ammonia in real-time [97].

The gas sensing properties of undoped and Graphene doped CuO-$SnO_2$**:**F samples were investigated. First, the optimum working temperature ($T_{work}$) of the samples was found at 250°C, and then all samples were exposed to different concentrations (5, 10, 20 and 25 ppm) of $NH_3$ gas for 1min.

The sensor response (S) is related to the type of sensitive material and the type of aimed gas (Table 5). In our case,it was calculated as follows [98]:

$$S = \frac{R_g}{R_0} \qquad (20)$$

Where $R_g$ is the sensor resistivity in the presence of $NH_3$ and $R_0$ is the initial sensor resistivity in the absence of the analyte.

Regarding the gas sensing performance, from Fig.13, it is well established that sensing response is related to dopant amount and it is evident that the highest response was presented by 6% graphene doped CuO-$SnO_2$:F sensor. This enhancement can be attributed to the presence of additional sites resulted from the surface defects and the large specific surface area, which are

promoted by the introduction of graphene. These sites are thermally activated and play crucial role in the ammonia ($NH_3$) adsorption process. In addition, this phenomena can be explained by the conductivity enhancement related to the strong interaction exhibited between graphene and CuO-$SnO_2$:F nanoparticles, which is correlated with impedance analysis.

Fig.14 displays the variation of the resistance of undoped (Fig.14.a) and 6% graphene doped CuO-$SnO_2$: F (Fig.14.b) at 250 °C towards different ammonia levels. It has been observed that sensor resistance increases upon exposure to ammonia gas and returns practically to its original value upon ammonia removal (p type behavior). CuO-$SnO_2$: F based sensor exhibits p-type conductivity under ambient conditions, it can transfer electrons to $O_2$ molecules adsorbed on its surface. The $NH_3$ sensing mechanism of undoped and graphene doped CuO-$SnO_2$:F thin films involves the following steps [99]:

$$O_2\ (gas) \rightarrow O_2\ (ads) \qquad (21)$$

$$O_2\ (ads) + e^- \rightarrow O_2^-\ (ads) \qquad (22)$$

$$O_2\ (ads) + 2\ e^- \rightarrow 2\ O^-\ (ads) \qquad (23)$$

$$O_2\ (ads) + 4\ e^- \rightarrow 2\ O^{2-}\ (ads) \qquad (24)$$

Depending on the working temperature, $O_2^-$, $O^-$, $O^{2-}$ oxygen species can adsorb onto the surface of our thin films [100]. Upon exposer to $NH_3$ in the temperature range of 200-300 °C (the operating temperature equals to 250 °C), the dominant oxygen species was $O^-$, as shown in (Eq.22). In our case, the reaction between $NH_3$ and CuO-$SnO_2$:F based sensor surface can be expressed as follow [101]:

$$3\ O^- + 2\ NH_3 \rightarrow N_2 + 3\ H_2O + 3\ e^- \qquad (25)$$

The electrons released during this reaction (Eq.25) combined with the holes of undoped and Graphene doped CuO-$SnO_2$:F samples, thereby reducing their hole concentrations and increasing their resistivity as seen in Fig.14.

To further investigation, the variation of response and recovery times of undoped and 6% graphene doped CuO-$SnO_2$:F sensors as a function of $NH_3$ concentration is displayed in Fig.15.Towards 5 ppm of $NH_3$ gas, the response and recovery times of 6% graphene doped CuO-$SnO_2$: F sensor were about 47 s and 62 s respectively while those of undoped CuO-$SnO_2$: F sensor were 133 s and 142 s respectively. However, the voids observed on the 6% graphene doped CuO-$SnO_2$: F thin films (Fig.2.b) helps the film to respond and recover faster. The faster performance is explained by the quick gas adsorption and desorption due to the higher surface area [102]. The 6% graphene-doped CuO-$SnO_2$:F thin films stand out due to their balance of good sensitivity, fast response and recovery times, which could lead to enhanced performance in real-world applications.

## 5. Conclusion

in this study, we explored the effect of graphene doping on the physical properties of CuO-$SnO_2$:F thin films produced by spray pyrolysis. Our findings show that 6% graphene-doped CuO-$SnO_2$:F films exhibit the best crystallinity, highest conductivity, and strongest absorbance in the visible region. Under sunlight, the photocatalytic performance of these films is impressive, with a degradation rate of 99% for methylene blue (MB), 87% for green malachite (GM), and 91% for rhodamine B (RdhB). Additionally, the graphene-doped thin films show superior sensing performance compared to the undoped films. Specifically, the 6% graphene-doped CuO-$SnO_2$:F sensor demonstrated enhanced sensitivity and faster response and recovery times (47 s and 62 s respectively) for low ammonia concentration of 5 ppm. These results

suggest that 6% graphene-doped CuO-$SnO_2$:F thin films have great potential for low-cost and eco-friendly applications in wastewater treatment and environmental monitoring of ammonia gas levels in the environment. Future research will focus on further optimizing the sample design exploring the synergetic effects of co-doping and investigating the long-term stability and the reliability. Additionally, efforts will be directed for enhanced performance and functionality by investigating on the design and the architecture of photocatalysis and gas sensing devices based on 6 % graphene-doped CuO-$SnO_2$:F thin films grown by spray pyrolysis.

**References:**

[1] Javan, Kazem, et al. "A review of interconnected challenges in the water–energy–food nexus: Urban pollution perspective towards sustainable development." *Science of The Total Environment* (2023) : 169319.

[2] Feng, Tong, et al. "Air pollution control policies and impacts: A review." Renewable and Sustainable Energy Reviews 191 (2024): 114071.

[3] Kumari, Diksha, et al. "Types and Sources of Agricultural Pollution: Identifying the different pollutants generated by farming practices and their origins." A Comprehensive Exploration of Soil, Water, and Air Pollution in Agriculture (2024): 71.

[4] Kolawole, Ayotunde Samuel, et al. "Environmental pollution: threats, impact on biodiversity, and protection strategies." Sustainable Utilization and Conservation of Africa's Biological Resources and Environment. Singapore: Springer Nature Singapore, 2023. 377-409.

[5] Morin-Crini, Nadia, et al. Worldwide cases of water pollution by emerging contaminants: a review. *Environmental Chemistry Letters*, 2022, 20.4: 2311-2338.

[6] Sahu, Pratyush Kumar, et al. "Design and development of nanostructured photocatalysts for large-scale solar green hydrogen generation." Sustainable Energy & Fuels 8.9 (2024): 1872-1917.

[7] Gopinath, Chinnakonda S, et al. A scalable and thin film approach for solar hydrogen generation: a review on enhanced photocatalytic water splitting. *Journal of Materials Chemistry A*, 2021, 9.3: 1353-1371.

[8] Danish, Mir Sayed Shah, et al. "Photocatalytic applications of metal oxides for sustainable environmental remediation." Metals 11.1 (2021): 80.

[9] Upadhyay, Ravi Kant, et al. "Role of graphene/metal oxide composites as photocatalysts, adsorbents and disinfectants in water treatment: a review." RSC advances 4.8 (2014): 3823-3851.

[10] Chaudhary, Ratiram Gomaji, et al. "Bioinspired graphene-based metal oxide nanocomposites for photocatalytic and electrochemical performances: an updated review." Nanoscale Advances (2024).

[11] Jamjoum, Hayfa Alajilani Abraheem, et al. "Synthesis, characterization, and photocatalytic activities of graphene oxide/metal oxides nanocomposites: A review." Frontiers in chemistry 9 (2021): 752276.

[12] Talukder, Niladri, et al. Nitrogen-doped graphene nanomaterials for electrochemical catalysis/reactions: A review on chemical structures and stability. *Carbon*, 2021, 185: 198-214.

[13] Jing, Erdong, et al. Dual redox catalysis of VN/nitrogen-doped graphene nanocomposites for high-performance lithium-sulfur batteries. *Journal of Energy Chemistry*, 2022, 64: 574-582.

[14] Guo, He, et al. Efficient removal of antibiotic thiamphenicol by pulsed discharge plasma coupled with complex catalysis using graphene-$WO_3$-$Fe_3O_4$ nanocomposites. *Journal of Hazardous Materials*, 2021, 403: 123673.

[15] Guo, He, et al. Multi-catalysis induced by pulsed discharge plasma coupled with graphene-$Fe_3O_4$ nanocomposites for efficient removal of ofloxacin in water: Mechanism, degradation pathway and potential toxicity. *Chemosphere*, 2021, 265: 129089.

[16] Yusuf, Bashir, et al. Efficiency improvement of molybdenum oxide doped with graphene oxide thin films solar cells processed by spray pyrolysis technique. *Physica B: Condensed Matter*, 2022, 625: 413532.

[17] Paul, John, et al. Photodegradation of methylene blue dye using graphene oxide incorporated, post-transition metal doped zinc oxide thin films by spray pyrolysis. *Physica Scripta*, 2024, 99.2: 025953.

[18] Luo, Manyu, et al. "Fast response/recovery and sub-ppm ammonia gas sensors based on a novel V 2 CT x@ MoS 2 composite." Journal of Materials Chemistry A 12.20 (2024): 12225-12236.

[19] Yuliarti, Rina, et al. Risk Analysis of Exposure to $NH_3$ And $H_2S$ Gas to Workers in The Small Industrial Environment of Magetan Regency in 2021. *International Journal of Advanced Health Science and Technology*, 2022, 2.3: 169-174.

[20] Bannov, Alexander G., et al. "Recent advances in ammonia gas sensors based on carbon nanomaterials." *Micromachines* 12.2 (2021): 186.

[21] Himabindu, Bantikatla, et al. "A nanostructured Al-doped ZnO as an ultra-sensitive room-temperature ammonia gas sensor." *Journal of Materials Science : Materials in Electronics* 34.12 (2023): 1014.

[22] Alagarasan, Devarajan, et al. Remarkable $NH_3$ gas sensing performance of spray deposited Tb doped $WO_3$ thin films at room temperature. *Journal of Photochemistry and Photobiology A: Chemistry*, 2025, 459: 116087.

[23] Fahad, Othman Abed, et al. Thin films of tungsten oxide based on $NH_3$ and $NO_2$ gas sensors. *Materials Today: Proceedings*, 2021, 42: 2405-2409.

[24] Anusha, et al. Evaluation of Zn: WO3 thin films as a sensing layer for detection of NH3 gas. *Micromachines*, 2023, 14.4: 732.

[25] Ravikumar, Thangavel, et al. "Substrate temperature dependent ammonia gas sensing performance of zinc ferrite thin films prepared by spray pyrolysis technique." Journal of Alloys and Compounds 959 (2023): 170568.

[26] Paul, Rinku, et al. "Novel approaches towards design of metal oxide based hetero-structures for room temperature gas sensor and its sensing mechanism: A recent progress." Journal of Alloys and Compounds 941 (2023): 168943.

[27] Sun, Dongjin, et al. "Graphene-enhanced metal oxide gas sensors at room temperature: A review." Beilstein journal of nanotechnology 9.1 (2018): 2832-2844.

[28] Salama, Tarek M., et al. "Synthesis of graphene oxide interspersed in hexagonal WO3 nanorods for high-efficiency visible-light driven photocatalysis and NH3 gas sensing." Frontiers in chemistry 7 (2019): 722.

[29] Ajili, Mejda, et al. "Structural, optical, photoluminescence and electrical properties of p-CuO/n-ZnO: Sn and p-CuO/n-α-Fe2O3 efficient hetero-junctions for optoelectronic applications." Journal of Luminescence 241 (2022): 118457.

[30] Sriram, Srinivasa Rao, et al. Prospects of spray pyrolysis technique for gas sensor applications–A comprehensive review. *Journal of Analytical and Applied Pyrolysis*, 2022, 164: 105527.

[31] Ajili, Mejda, et al. "Spray solution flow rate effect on growth, optoelectronic characteristics and photoluminescence of $SnO_2$: F thin films for photovoltaic application." *Optik* 126.7-8 (2015): 708-714.

[32] Charrada, Ghofrane, et al. "Investigation on physical properties of CuO and $SnO_2$: F mixed oxide sprayed thin films for photocatalytic application: coupling effect between oxides." Journal of Materials Science : Materials in Electronics 35.10 (2024): 685.

[33] Charrada, Ghofrane, et al. "Improvement of ozone sensing parameters by CuO–$SnO_2$: F mixed oxide sprayed thin films." *Journal of Materials Science: Materials in Electronics* 35.17 (2024): 1120.

[34] Charrada, Ghofrane, et al. "Unlocking the potential of CIGS solar cells: harnessing CZTS as a second absorber layer for enhanced performance and sustainability." *Journal of Optics* (2024): 1-10.

[35] Charrada, Ghofrane, et al. Investigation on thermal annealing effect on the physical properties of CuO-$SnO_2$: F sprayed thin films for $NO_2$ gas sensor and solar cell simulation. *Materials Letters*, 2024, 367: 136666.

[36] Blau, Rachel, et al. "Surface-Grafted Biocompatible Polymer Conductors for Stable and Compliant Electrodes for Brain Interfaces." *Advanced Healthcare Materials* (2024): 2402215.

[37] Yang, Dongchang, et al. "Nanomaterials for surface-enhanced Raman spectroscopy-based metal detection: a review." *Environmental Chemistry Letters* (2024): 1-41.

[38] Hajji, Moez, et al. Photocatalytic performance and solar cell applications of coupled semiconductor CuO–ZnO sprayed thin films: Coupling effect between oxides. *Optical Materials*, 2023, 140: 113798.

[39] Karyaoui, M., et al. "Physical properties of graphene oxide GO-doped ZnO thin films for optoelectronic application." *Applied Physics A* 127 (2021): 1-14.

[40] Kamoun, Olfa, et al. "Synthesis and characterization of highly photocatalytic active Ce and Cu Co-doped novel spray pyrolysis developed $MoO_3$ films for photocatalytic degradation of eosin-Y dye." *Coatings* 12.6 (2022): 823.

[41] Yahmadi, Bechir, et al. "Physical investigations of (Co, Mn) Co-doped ZnO nanocrystalline films." *Nanomaterials* 10.8 (2020): 1507.

[42] Solangi, Nadeem Hussain, et al. "Recent development of graphene and MXene-based nanomaterials for proton exchange membrane fuel cells." *International Journal of Hydrogen Energy* 73 (2024): 905-931.

[43] Chai, Hongfeng, et al. Stability of metal oxide semiconductor gas sensors: A review. *IEEE Sensors Journal*, 2022, 22.6: 5470-5481.

[44] Isaac, N. A, et al. Metal oxide semiconducting nanomaterials for air quality gas sensors: operating principles, performance, and synthesis techniques. *Microchimica Acta*, 2022, 189.5: 196.

[45] Bellal, Youcef, et al. $CuO/SnO_2$ nanocomposite thin films: effect of solvent and precursor on optical and structural properties. *International Journal of Nanoscience*, 2021, 20.03: 2150029.

[46] Cynthia, S. R, et al. Ternary CuO: $SnO_2$: ZnO (1: 1: 1) composite thin film for room temperature gas sensor application. *Optik*, 2021, 234: 166615.

[47] Huang, Pei, et al. "Graphene film for thermal management: A review." Nano Materials Science 3.1 (2021): 1-16.

[48] Mirzaei, Ali, et al. Metal oxide semiconductor nanostructure gas sensors with different morphologies. *Chemosensors*, 2022, 10.7: 289.

[49] Bi, Han, et al. Morphology-controlled synthesis of $CeO_2$ nanocrystals and their facet-dependent gas sensing properties. *Sensors and Actuators B: Chemical*, 2021, 330: 129374.

[50] Liu, Xianghong, et al. Conducting polymer-based nanostructures for gas sensors. *Coordination Chemistry Reviews*, 2022, 462: 214517.

[51] Chowdhury, N. K, et al. Micro/nanostructured gas sensors: the physics behind the nanostructure growth, sensing and selectivity mechanisms. *Nanoscale Advances*, 2021, 3.1: 73-93.

[52] Li, Jin, et al. Ultrafast response and high-sensitivity acetone gas sensor based on porous hollow Ru-doped $SnO_2$ nanotubes. *Sensors and Actuators B: Chemical*, 2022, 352: 131061.

[53] Faisala, D., et al. Synthesis of $CuO/SnO_2$ NPs on quartz substrate for temperature sensors application. *parameters*, 2022, 20: 19.

[54] Imen Ammar, et al, Deposition of SnS thin films by chemical bath deposition method: Effect of surfactants, The European Physical Journal Plus, Volume 134, article number 505, (2019).

[55] Souli, Mehdi, et al. "Physical properties investigation of samarium doped calcium sulfate thin films under high gamma irradiations for space photovoltaic and dosimetric applications." Superlattices and Microstructures 126 (2019): 103-119.

[56] Hajji, Moez, et al. Bismuth doping for enhanced physical and electrochemical properties of CuO–ZnO thin films for complete degradation of Rifampicin and other antibiotics alongside organic dyes. *Optical Materials*, 2024, 157: 116048.

[57] Rahman, Nasir, et al. "Insight into metallic oxide semiconductor ($SnO_2$, ZnO, CuO, α-$Fe_2O_3$, $WO_3$)-carbon nitride (g-$C_3N_4$) heterojunction for gas sensing application." *Sensors and Actuators A: Physical* 332 (2021): 113128.

[58] Masudy-Panah, Saeid, et al. "Graphene nanoparticle incorporated CuO thin film for solar cell application." *Journal of Renewable and Sustainable Energy* 8.4 (2016).

[59] Mobasheri, Abbas, et al. Cd-doped $SnO_2$-reduced graphene oxide composite nanofibrous mats as CO gas sensors. *Fibers and Polymers*, 2022, 23.3: 784-790.

[60] Zhao, Chenxi, et al. Burstein-moss effect leads to an unusual suppression of bipolar conduction with shrinking bandgap. *Journal of Materials Chemistry A*, 2024, 12.35: 23670-23675.

[61] Ivchenko, Vladimir. Theory of Burstein-Moss effect in semiconductors with anisotropic energy bands. *Physica Scripta*, 2024, 99.3: 035952.

[62] Zaidi, Beddiaf, et al. Synthesis, Characterization, and Photocatalytic Performance of (Eu, Ni) Co-Doped ZnO Thin Films for Environmental Applications. *Journal of Nano Research*, 2024, 86: 77-88.

[63] Jrad, Abdelhak, et al. "Investigation of molybdenum dopant effect on ZnS thin films: Chemical composition, structural, morphological, optical and luminescencsurveys." *Materials science in semi-conductor processing* 130 (2021): 105825.

[64] Akkari, Anis, et al. "Optical study of zinc blend SnS and cubic $In_2S_3$: Al thin films prepared by chemical bath deposition." *Journal of materials science* 46 (2011): 6285-6292.

[65] Mandal, Pramod, et al. Optical performance of europium-doped β gallium oxide PVD thin films. *Journal of Materials Science: Materials in Electronics*, 2021, 32: 3958-3965.

[66] Cheng, Zhaoyang, et al. Cobalt-Catalyzed Regiodivergent Double Hydrosilylation of Arylacetylenes. *Angewandte Chemie*, 2023, 135.1: e202215029.

[67] Plajer, Alex J.; Williams, Charlotte K. Heterocycle/Heteroallene Ring-Opening Copolymerization: Selective Catalysis Delivering Alternating Copolymers. *Angewandte Chemie International Edition*, 2022, 61.1: e202104495.

[68] Saad, Haifa Ben, et al. Investigation on thickness and annealing effects on physical properties and electrical circuit model of CuO sprayed thin films. *Superlattices and Microstructures*, 2020, 142: 106508.

[69] Ajili, Mejda, et al. Investigation on substrate effect on physical characteristics of CuO-sprayed thin films suitable for photovoltaic application: Ag/ZnO: Sn (n)/CuO (p)/$SnO_2$: F. *Materials Technology*, 2022, 37.6: 381-396.

[70] Ayed, Rihab Ben, et al. Substrate temperature effect on the crystal growth and optoelectronic properties of sprayed α-$Fe_2O_3$ thin films: application to gas sensor and novel photovoltaic solar cell structure. *Materials Technology*, 2018, 33.12: 769-783.

[71] Ayed, Rihab Ben, et al. Physical properties investigation and gas sensing mechanism of Al: $Fe_2O_3$ thin films deposited by spray pyrolysis. *Superlattices and Microstructures*, 2019, 129: 91-104.

[72] Sambyal, Shabnam, et al. "Advancement in two-dimensional carbonaceous nanomaterials for photocatalytic water detoxification and energy conversion." *Journal of Environmental Chemical Engineering* 11.2 (2023): 109517.

[73] Yang, Xinxiu, et al. "Research Progress of Graphene and Its Derivatives towards Exhaled Breath Analysis." *Biosensors* 12.2 (2022): 48.

[74] Kerli, Süleyman, et al. Photocatalytic degradation of methylene blue, rhodamine-B, and malachite green by Ag@ ZnO/$TiO_2$. *Brazilian Journal of Physics*, 2022, 52.1: 22.

[75] Pedanekar, R. S et al. Thin film Photocatalysis for environmental remediation: A status review. *Current Applied Physics*, 2020, 20.8: 931-952.

[76] Sarathi, R., et al. Photocatalytic degradation of malachite green dye by metal oxide nanoparticles-mini review. *J. Chem. Rev*, 2023, 5.1: 15-30.

[77] Aghaei, M., et al. Review of degradation and failure phenomena in photovoltaic modules. *Renewable and Sustainable Energy Reviews*, 2022, 159: 112160.

[78] Hosseini, Ali, et al. Heterogeneous photoelectro-Fenton using ZnO and $TiO_2$ thin film as photocatalyst for photocatalytic degradation Malachite Green. *Applied Surface Science Advances*, 2021, 6: 100126.

[79] Yusuf, Tunde Lewis, et al. The application of photoelectrocatalysis in the degradation of rhodamine B in aqueous solutions: A review. *RSC advances*, 2022, 12.40: 26176-26191.

[80] Hajji, Moez, et al. "Advanced oxidation processes (AOPs): Navigating from MOS to COS and X-COS systems-Unravelling strategies, tackling challenges, and pioneering advances." *Optical Materials* 152 (2024): 115399.

[81] Hammoud, Amal, et al. "Impact of sprayed volume on physical properties of $Cu_2MgSnS_4$ thin film for photocatalytic and humidity sensing applications." *The European Physical Journal Plus* 138.11 (2023): 1008.

[82] Andoni, Ilektra, et al. Investigating the degradation of $Nb_2O_5$ thin films across 10,000 lithiation/delithiation cycles. *ACS Applied Energy Materials*, 2021, 4.7: 6542-6552.

[83] Bao, Fuxi, et al. Host, suppressor, and promoter—the roles of Ni and Fe on oxygen evolution reaction activity and stability of NiFe alloy thin films in alkaline media. *ACS Catalysis*, 2021, 11.16: 10537-10552.

[84] Pérez-Gonzalez, M.; TOMÁS, S. A. Surface chemistry of $TiO_2$-ZnO thin films doped with Ag. Its role on the photocatalytic degradation of methylene blue. *Catalysis Today*, 2021, 360: 129-137.

[85] Anucha, Chukwuka Bethel, et al. Titanium dioxide ($TiO_2$)-based photocatalyst materials activity enhancement for contaminants of emerging concern (CECs) degradation: In the light of modification strategies. *Chemical Engineering Journal Advances*, 2022, 10: 100262.

[86] T. Pham, C, et al Author ' s Accepted Manuscript, Ceram. Int. (2015).

[87] L. Xu, et al. Materials Science & Engineering B Enhanced photocatalytic performance of porous ZnO thin films by CuO nanoparticles surface modification, 248 (2019).

[88] K. Ravichandran, S. Porkodi, Addressing the issue of under-utilization of precursor material in SILAR process: Simultaneous preparation of CdS in two different forms – Thin film and powder, Mater. Sci. Semicond. Process. 81 (2018) 30–37.

[89] Al-Mousawi, Rawasi Ayad, et al. Activity $SnO_2$/CuO nanocomposite toward photocatalytic degradation of methylene blue dye under solar light. In: *AIP Conference Proceedings*. AIP Publishing, 2024.

[90] Vomacka, Petr, et al. Shape-controlled synthesis of Sn-doped CuO nanoparticles for catalytic degradation of Rhodamine B. *Journal of colloid and interface science*, 2016, 481: 28-38.

[91] Wang, J, et al. Synthesis of Hierarchical $SnO_2$ Microflowers Assembled by Nanosheets and Their Enhanced Photocatalytic Properties. Mater. Trans. 2015, 56, 1911–1914

[92] Xiao, Bing, et al. Facile synthesis of CuO nanosheets and efficient degradation of rhodamine B in a copper oxide/ascorbic acid/hydrogen peroxide system: Kinetics, fate of ascorbic acid, and mechanism. *ChemistrySelect*, 2020, 5.20: 6075-6082.

[93] Sankaran, A.; KUMARAGURU, K. The novel two step synthesis of CuO/ZnO and CuO/CdO nanocatalysts for enhancement of catalytic activity. *Journal of Molecular Structure*, 2020, 1221: 128772.

[94] Kumaravelan, S., et al. Effect of Zn dopant on $SnO_2$ nano-pyramids for photocatalytic degradation. *Chemical Physics Letters*, 2021, 769: 138352.

[95] Senthilkumar, P., et al. Optoelectronic, photocurrent sensitivity and photocatalytic dye degradation behavior of spray deposited Cr doped $SnO_2$ thin films. *Materials Chemistry and Physics*, 2023, 305: 127988.

[96] Ni, Zhenyi, et al. Evolution of defects during the degradation of metal halide perovskite solar cells under reverse bias and illumination. *Nature Energy*, 2022, 7.1: 65-73.

[97] Yuliarti, Rina, et al. Risk Analysis of Exposure to $NH_3$ And $H_2S$ Gas to Workers in The Small Industrial Environment of Magetan Regency in 2021. *International Journal of Advanced Health Science and Technology*, 2022, 2.3: 169-174.

[98] Hidayatullah, Farisa, et al. Health Risk Analysis of Hydrogen Sulfide ($H_2S$) and Ammonia ($NH_3$) Exposure at Piyungan Landfill. *Environmental & Earth Sciences Research Journal*, 2021, 8.1.

[99] Ahmed, Sarfraj, and Sudip K. Sinha. "Studies on nanomaterial-based p-type semiconductor gas sensors." *Environmental Science and Pollution Research* 30.10 (2023): 24975-24986.

[100] G. Korotcenkov, et al, $In_2O_3$- and $SnO_2$-based ozone sensors: design and characterization,Crit. Rev. Solid State Mater. Sci., 43 (2018), pp. 83-132.

[101] Athanasios Paralikis, et al, Study on the Ozone Gas Sensing Properties of rf-Sputtered Al-Doped NiO Films, Appl. Sci. 2021, 11(7), 3104.

[102] Alturaifi, Sulaiman A., et al. "A shock-tube study of $NH_3$ and $NH_3/H_2$ oxidation using laser absorption of $NH_3$ and $H_2O$." *Proceedings of the Combustion Institute* 39.1 (2023): 233-241.

**Figure captions:**

Figure.1: X-ray diffraction patterns of undoped and Gr-doped CuO-$SnO_2$:F thin films.

Figure.2: SEM images at two scales (1 μm and 300 nm) of (a) undoped and (b) 6% Gr-doped CuO-$SnO_2$:F thin films. Elemental mapping images of (c) Copper (Cu) and (d) Tin (Sn) in CuO-$SnO_2$:F thin films . TEM images at 10 nm of (e) undoped and (f) 6% Gr-doped CuO-$SnO_2$:F thin films.

Figure 3:(a) The transmission (T) and (b) reflection (R) spectrum of undoped and Gr-doped CuO-$SnO_2$: F thin films.

Figure 4: Tauc's plots for CuO and $SnO_2$ band gap energies of undoped and Gr-doped CuO-$SnO_2$: F thin films.

Figure 5: Plots of dT/dλ versus λ curves of undoped and Gr-doped CuO-$SnO_2$:F thin films.

Figure 6: Influence of Gr doping level on the band gap of CuO and $SnO_2$ phases in CuO-$SnO_2$:F nanocomposites.

Figure 7: (a) The refractive index n and (b) the extinction coefficient k spectra as a function of wavelength of undoped and Gr-doped CuO-$SnO_2$: F thin films.

Figure.8: (a)The equivalent circuit for the experimental data of the impedance spectroscopy, Nyquist plot of complex impedance spectra of undoped (b) and Gr-doped CuO-$SnO_2$: F thin films(c).

Figure.9:Absorbance spectra of diverse pollutants ((a) methylene blue (MB),(b)green malachite (GM)and(c) rhodamine B (RdhB)) using various catalysts (undoped and graphene doped CuO-$SnO_2$:F thin films at different graphene concentration).

Figure.10:Ln(C/ $C_0$) spectra of diverse pollutants((a) methylene blue (MB), (b) green malachite (GM) and (c) rhodamine B (RdhB)) using various catalysts (undoped and graphene doped CuO-$SnO_2$:F thin films at different graphene concentration).

Figure.11: The rate constants spectra of diverse pollutants( methylene blue (MB), green malachite (GM) and rhodamine B (RdhB)) using various catalysts (undoped and graphene doped CuO-$SnO_2$:F thin films at different graphene concentration).

Figure.12: Photodegradation rates of various pollutants and at various irradiation time ((a) methylene blue (MB), (b) green malachite (GM) and (c) rhodamine B (RdhB)) using various catalysts (undoped and graphene doped CuO-$SnO_2$:F thin films at different graphene concentration).

Figure.13: Gas sensor response of undoped and Gr-doped CuO-$SnO_2$:F samples exposed to 25 ppm of $NH_3$ gas at 250°C as a function of time.

Figure.14: Real-time resistance variation curves of the gas sensors based on (a) Undoped and (b) 6% Gr-doped CuO-$SnO_2$:F thin films to 5–25 ppm $NH_3$at 250°C.

Figure.15: Variation of response and recovery times of undoped and 6% Gr-doped CuO-$SnO_2$:F thin films sensors with $NH_3$ gas concentrations.

**Table captions:**

Table 1: structural (D and δ are the crystallite size and the dislocation density) and electrical parameters (R1, R 2 and C1 are respectively a series resistance, a parallel resistance and the capacitance) for different synthesized thin films.

Table 2:The estimated values of band gap energy ($E_g$) for undoped and Gr-doped CuO-$SnO_2$: F thin films.

Table 3: Rate constant (k) and degradation efficiency of diverse pollutants (Methylene blue (MB), green malachite (GM) and rhodamine B (RdhB)) using undoped and Gr-doped CuO-$SnO_2$: F thin films as a catalyst.

Table 4: Comparison table for degradation of methylene blue (MB) , rhodamine B(RdhB) and green malachite (GM) pollutants using various catalysts.

Table 5: Sensitivity parameters of material type and target gas type.

**Table 1**

| **Thin film** | **D(nm)** | **δ (*$10^{-4}$nm$^{-2}$)** | **$R_1$(kΩ)** | **$R_2$(kΩ)** | **$C_1$** |
|---|---|---|---|---|---|
| Undoped CuO-$SnO_2$:F | 10 | 100 | 351.691 | 24175 | $2.8x10^{-12}$ |
| 2 % Gr doped CuO-$SnO_2$:F | 11 | 82.6 | 4.5 | 1124 | $2.67x10^{-12}$ |
| 4 % Gr doped CuO-$SnO_2$:F | 13 | 59.2 | 3.163 | 276.720 | $3.65x10^{-11}$ |
| 6 % Gr doped CuO-$SnO_2$:F | 21 | 22.7 | 0.878 | 63.852 | $1.55x10^{-11}$ |

**Table 2**

| Thin Film | $E_g$ :Band gap Energy (eV) | | | |
|---|---|---|---|---|
| | Defferentiate method | | Tauc method | |
| | CuO phase | $SnO_2$ phase | CuO phase | $SnO_2$ phase |
| Undoped CuO-SnO2 : F | 1.501 | 3.092 | 1.501 | 3.088 |
| 2 % Gr doped CuO-SnO2 :F | 1.499 | 2.743 | 1.50 | 2.749 |
| 4 % Gr doped CuO-SnO2 :F | 1.497 | 2.393 | 1.499 | 2.390 |
| 6 % Gr doped CuO-SnO2 :F | 1.449 | 2.242 | 1.45 | 2.238 |

**Table 3**

| Sample | Rate Constant k | | | Efficiency (%) | | |
|---|---|---|---|---|---|---|
| | MB | GM | RdhB | MB | GM | RdhB |
| Undoped CuO-$SnO_2$:F | 0.0065 | 0.0043 | 0.0054 | 73 | 72 | 71 |
| 2 % Gr doped CuO-$SnO_2$:F | 0.007 | 0.0055 | 0.0066 | 88 | 76 | 80 |
| 4 % Gr doped CuO-$SnO_2$:F | 0.0099 | 0.0078 | 0.0081 | 94 | 80 | 83 |
| 6 % Gr doped CuO-$SnO_2$:F | 0.012 | 0.0088 | 0.0094 | 99 | 87 | 91 |

**Table 4**

| Sample | Pollutant | Degradation Efficiency(%) | Time (min) | Reference |
|---|---|---|---|---|
| Cu-doped $TiO_2$/reduced graphene oxide | MB | 63 | 180 | [88] |
| CuO nanoparticals modified ZnO | MB | 84 | 120 | [89] |
| CdS | MB | 89 | 120 | [90] |
| CuO-$SnO_2$ | MB | 96 | 135 | [91] |
| CuO nanosheets | RdhB | 24 | 120 | [91] |
| $SnO_2$ multilayered films | RdhB | 80 | 180 | [91] |
| CuO combined with trace of ascorbic acid | RdhB | 80 | 100 | [92] |
| CuO-CdO | RdhB | 73.15 | 120 | [93] |
| CuO-CdO | GM | 74.69 | 120 | [93] |
| CuO-ZnO | GM | 79.82 | 120 | [93] |
| SnO2:Zn | GM | 87 | 180 | [94] |
| Cr doped $SnO_2$ | GM | 63 | 180 | [95] |
| 6%Gr doped CuO-$SnO_2$:F | MB | 99 | 120 | our work |
| 6%Gr doped CuO-$SnO_2$:F | GM | 87 | 120 | our work |
| 6%Gr doped CuO-$SnO_2$:F | RdhB | 91 | 120 | our work |

**Table 5**

| Type of sensitive material | Type of aimed gas | Response (S) |
|---|---|---|
| **n-type** | Oxidizing | $R_g/R_0$ |
| | reducing | $R_0/R_g$ |
| **p-type** | Oxidizing | $R_0/R_g$ |
| | reducing | $R_g/R_0$ |

**Figure 1**

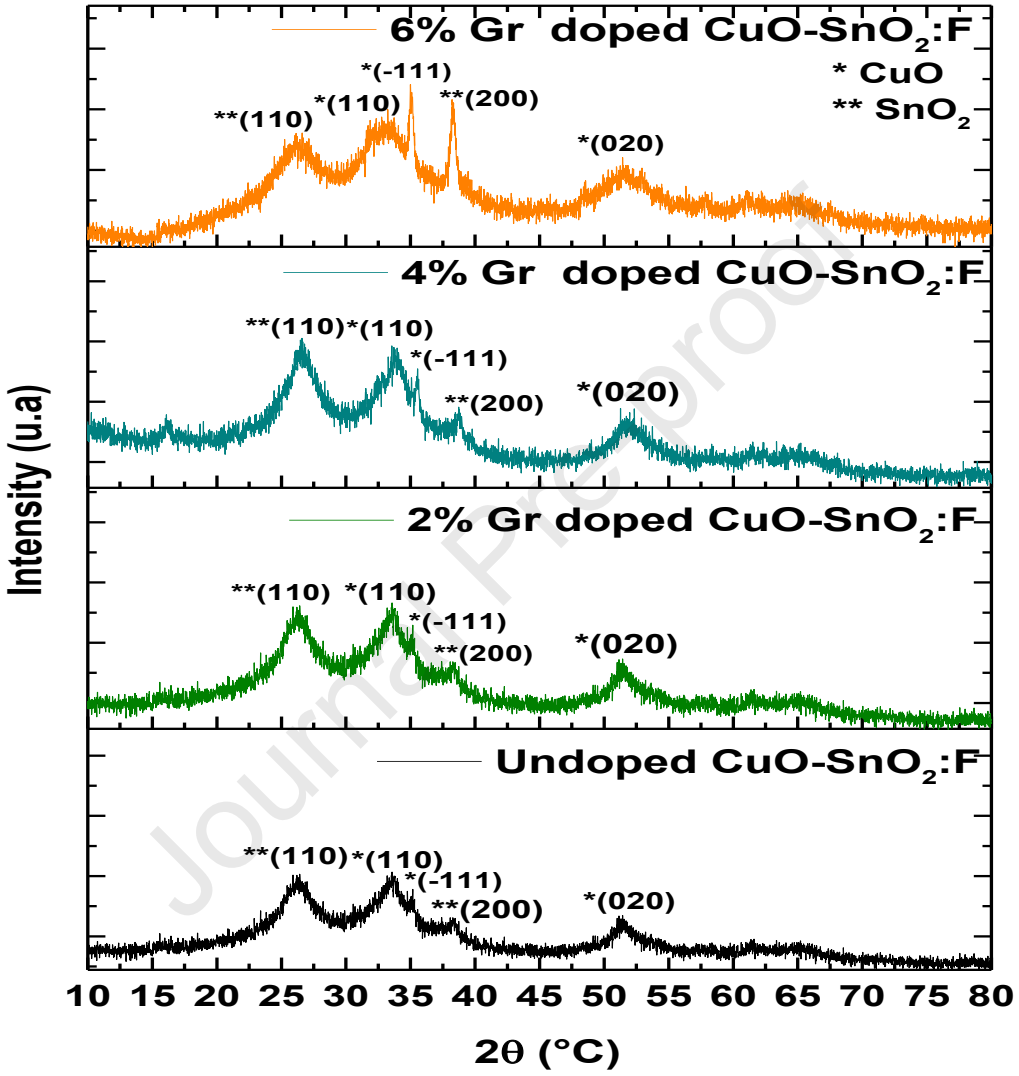

**Figure 2**

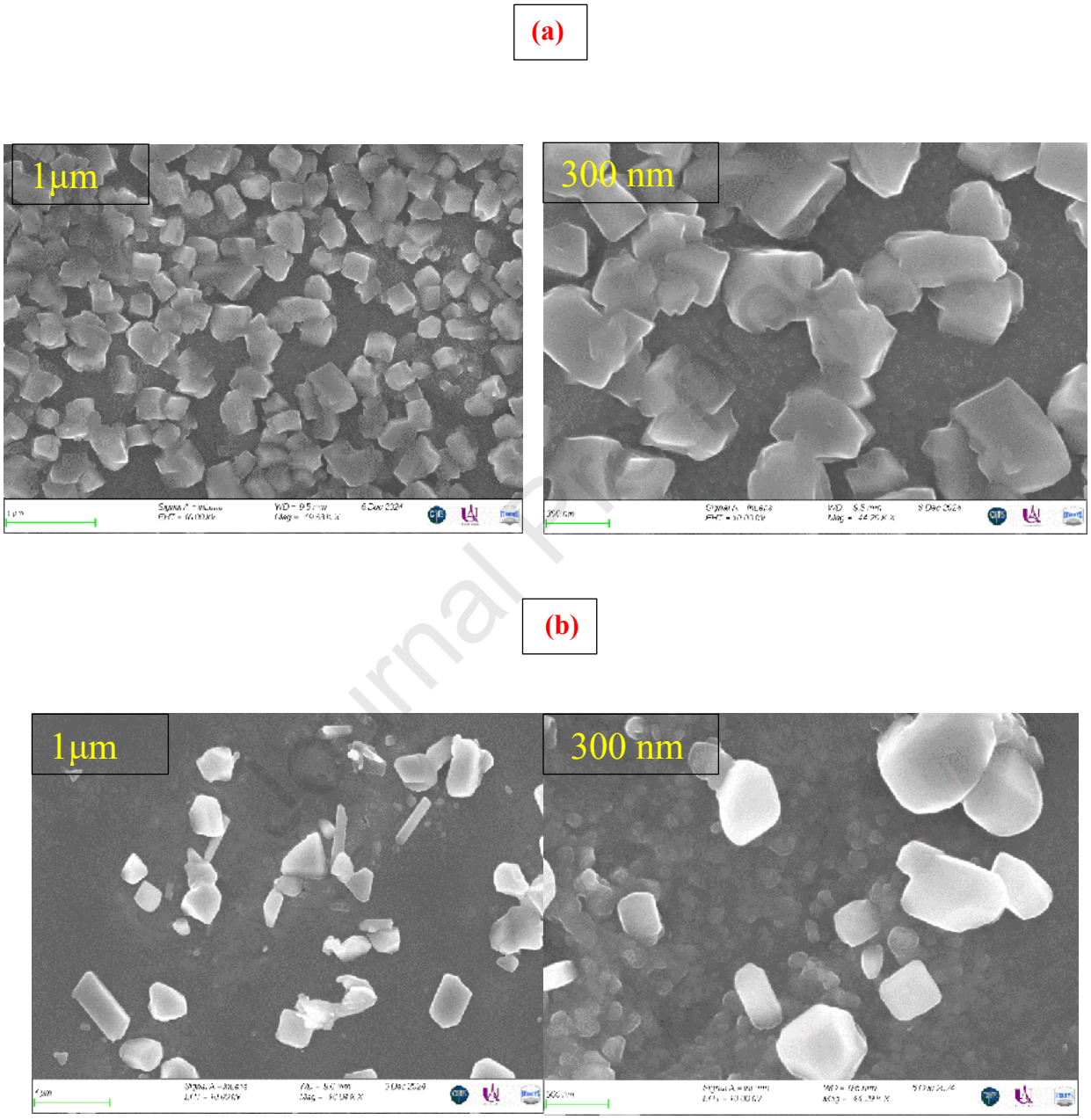

(c)

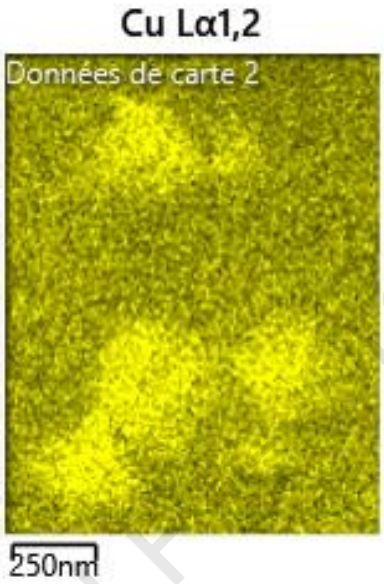


(d)

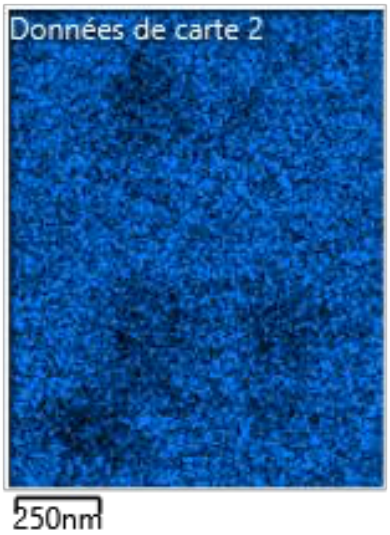

(e)

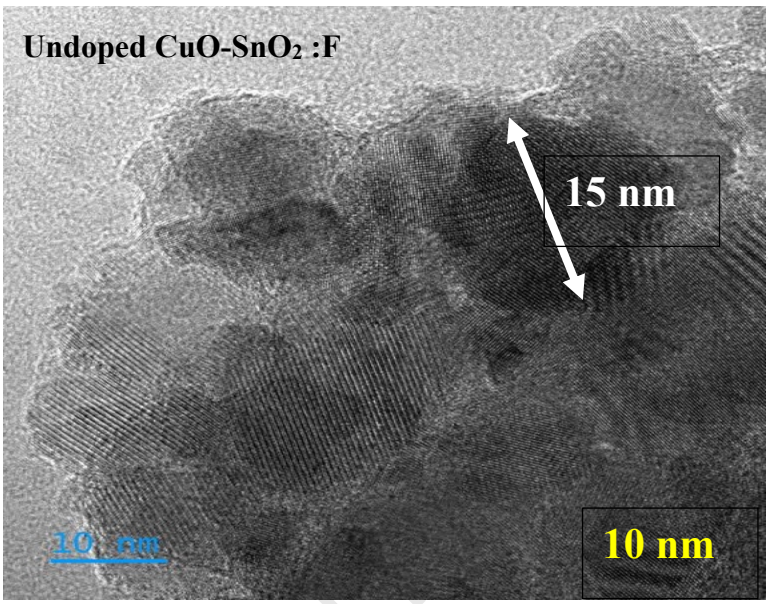


(f)

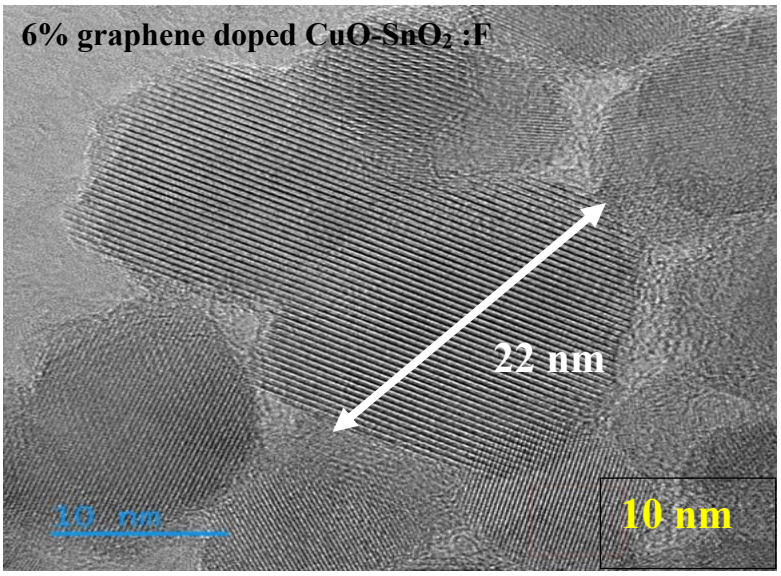

**Figure 3**

**(a)**

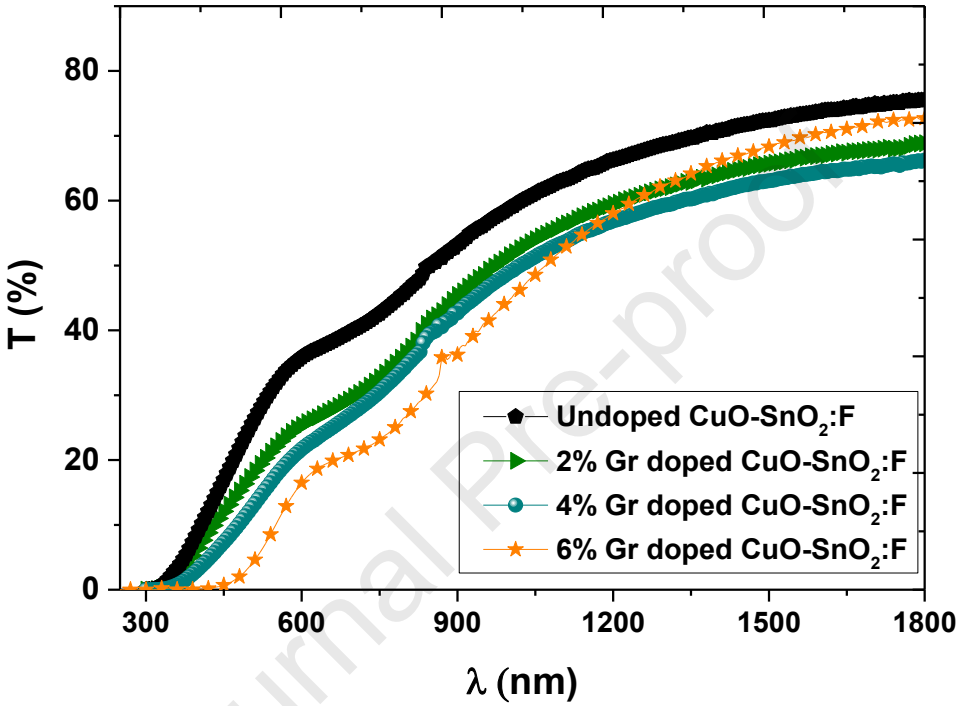

**(b)**

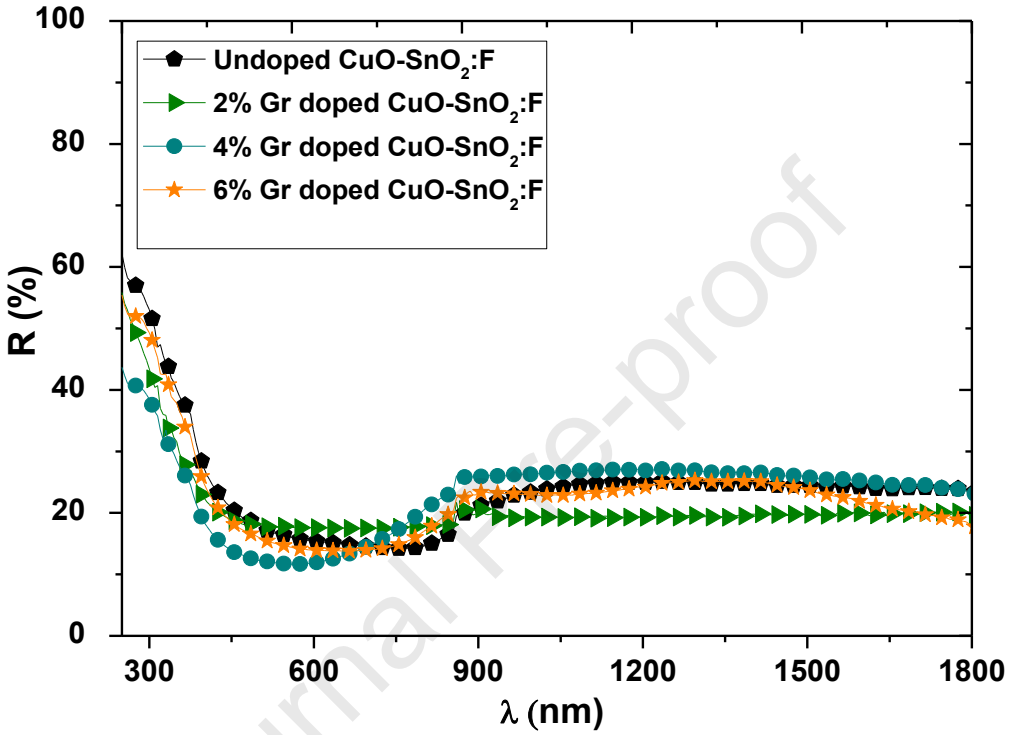

**Figure 4**

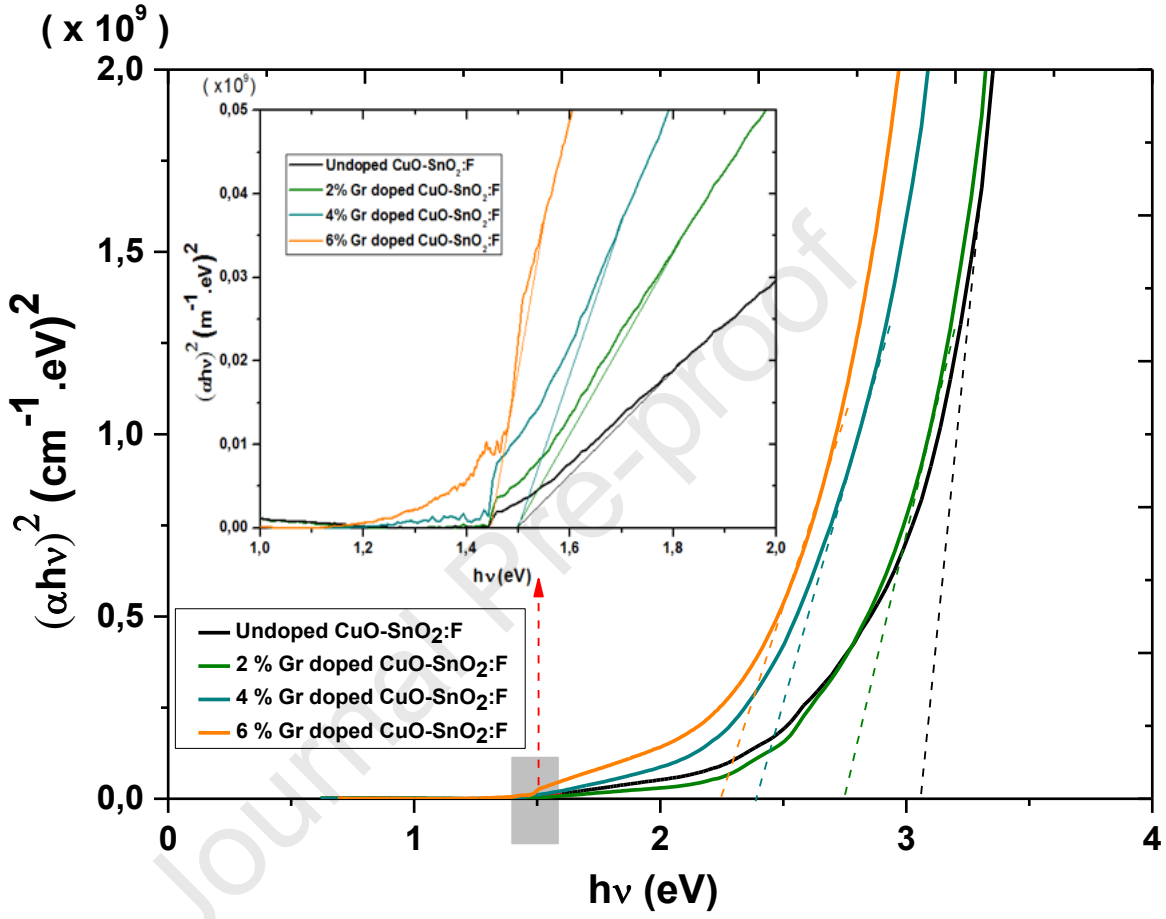

**Figure 5**

**(a)**

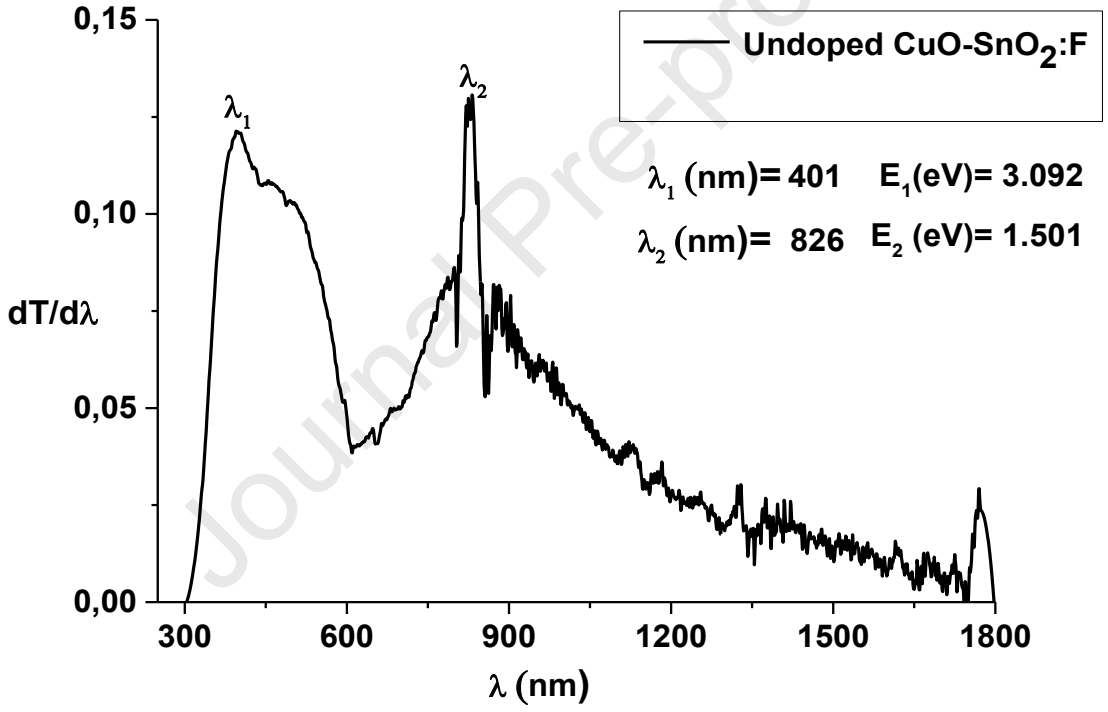

**(b)**

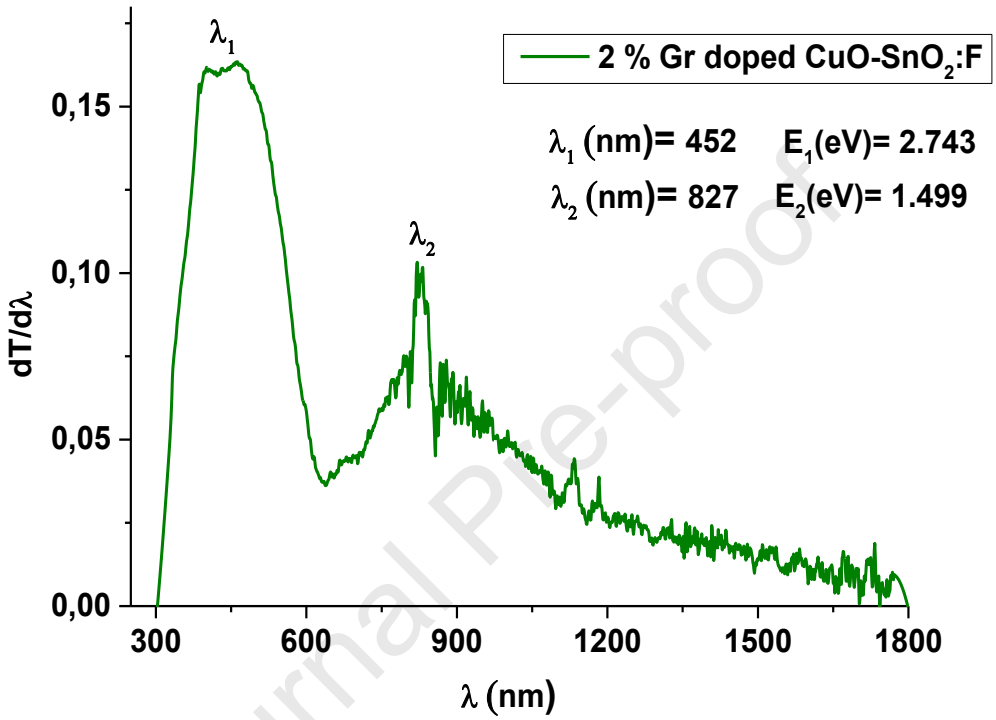

**(c)**

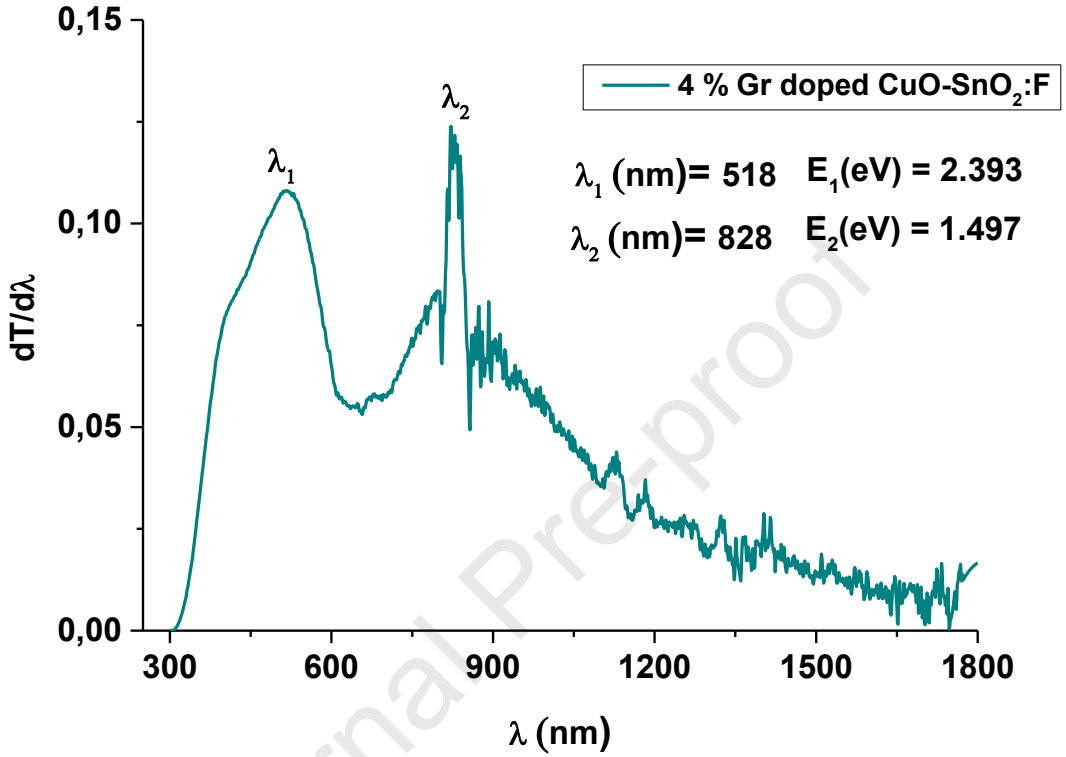

**(d)**

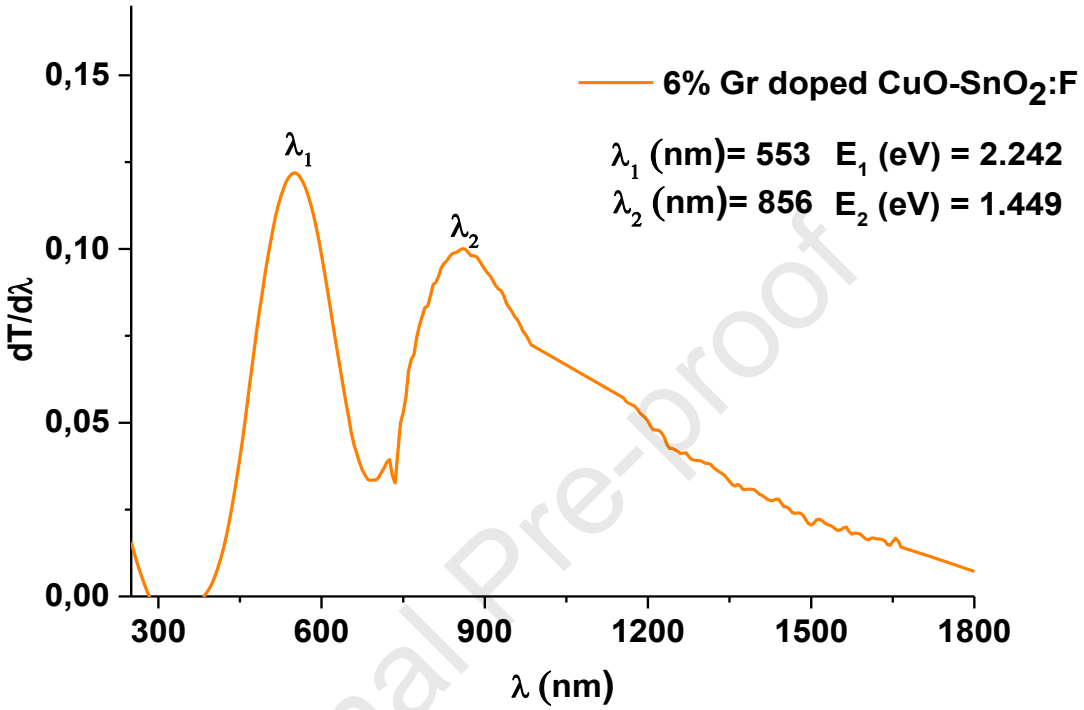

**Figure 6**

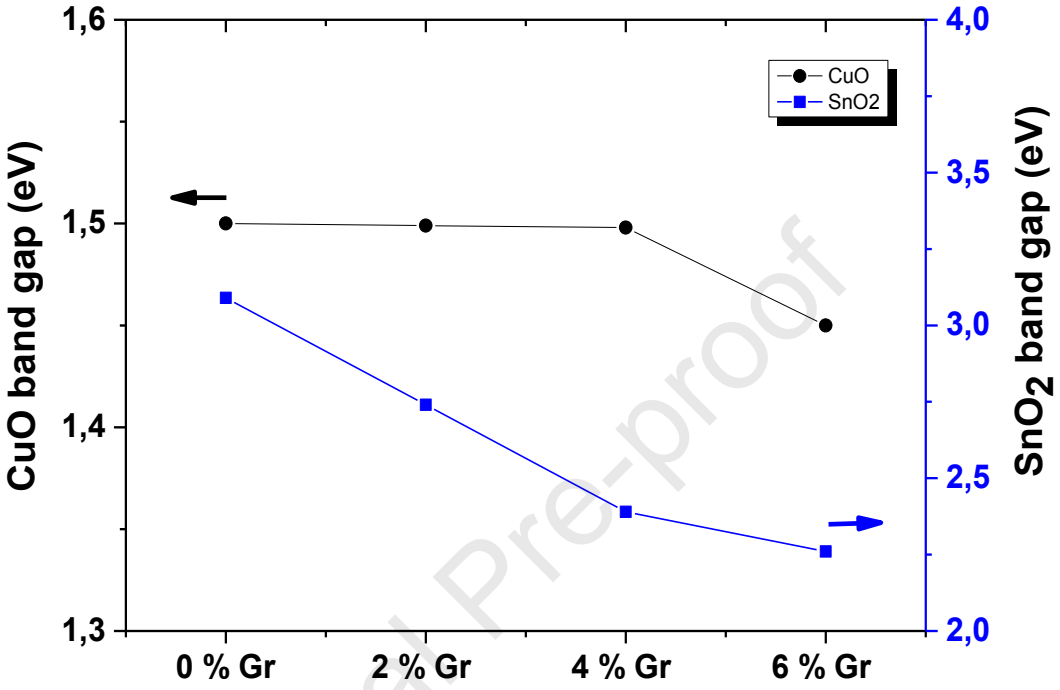

**Figure 7**

**(a)**

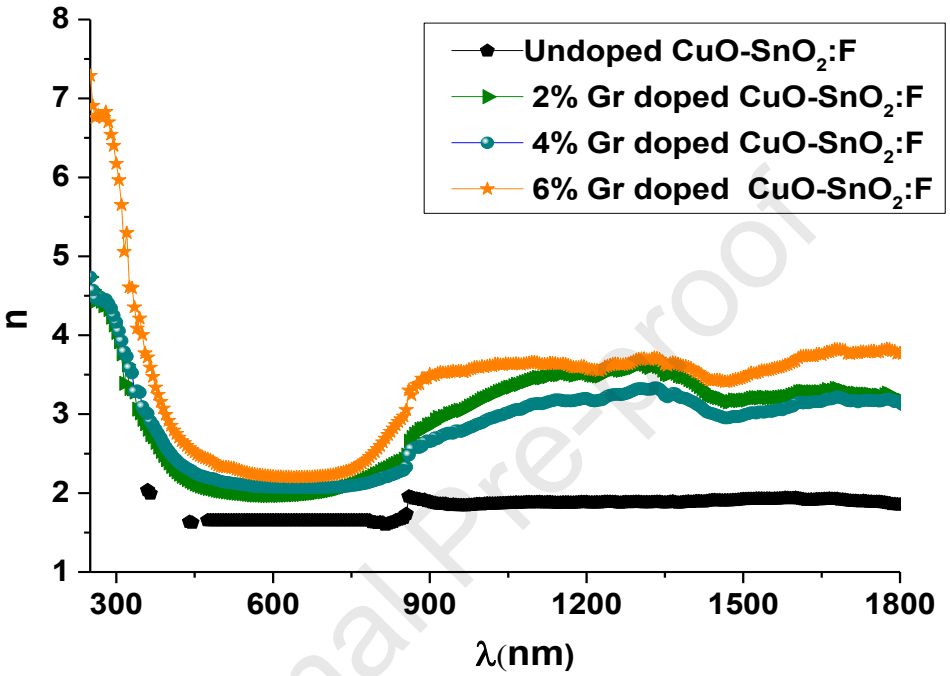

**(b)**

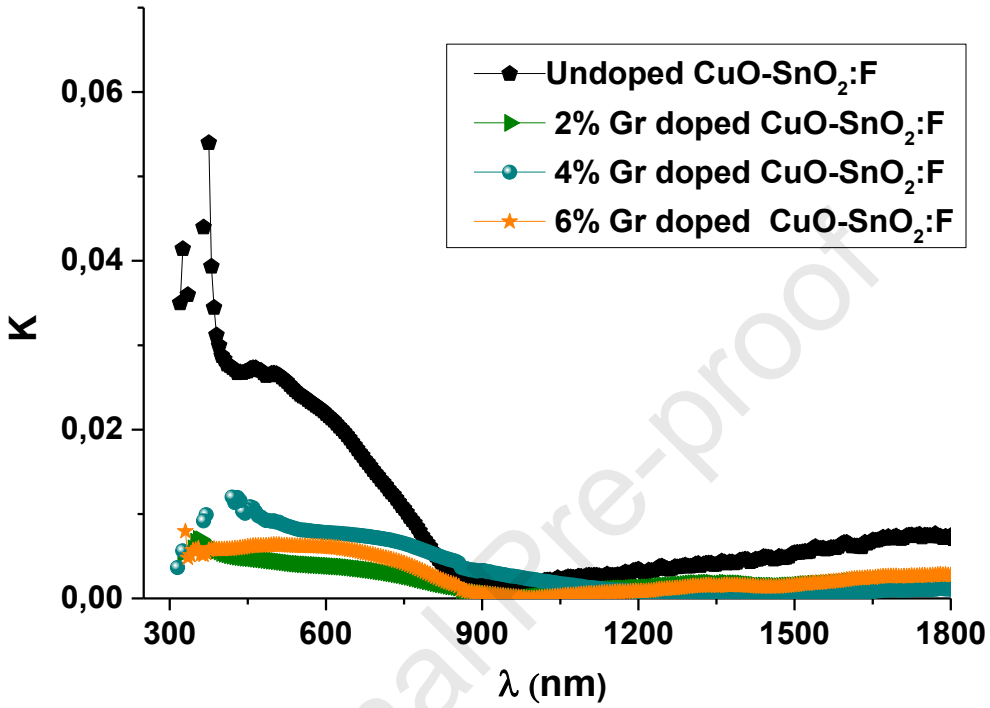

**Figure 8**

**(a)**




**(b)**

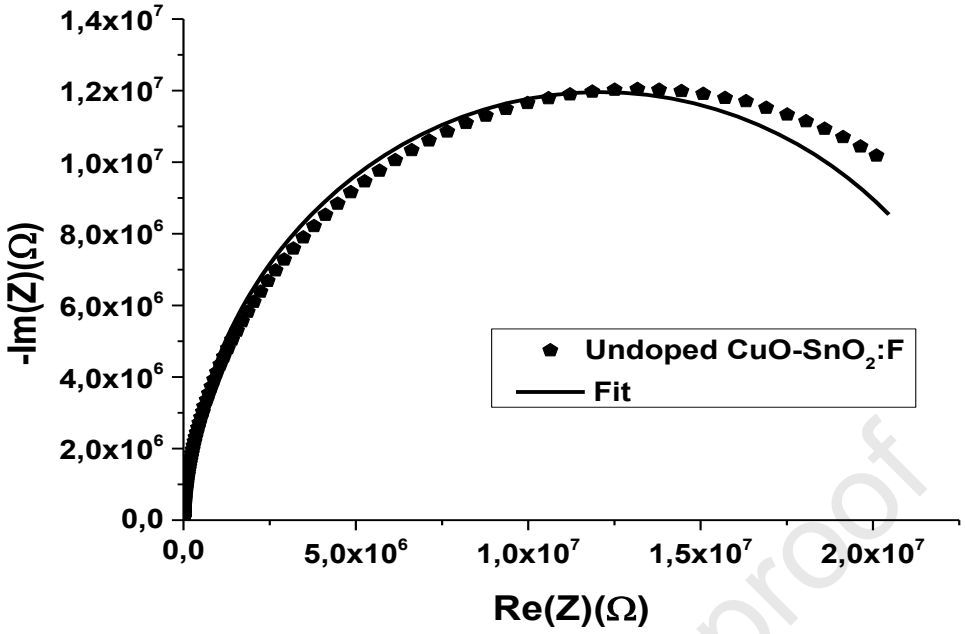




**(c)**

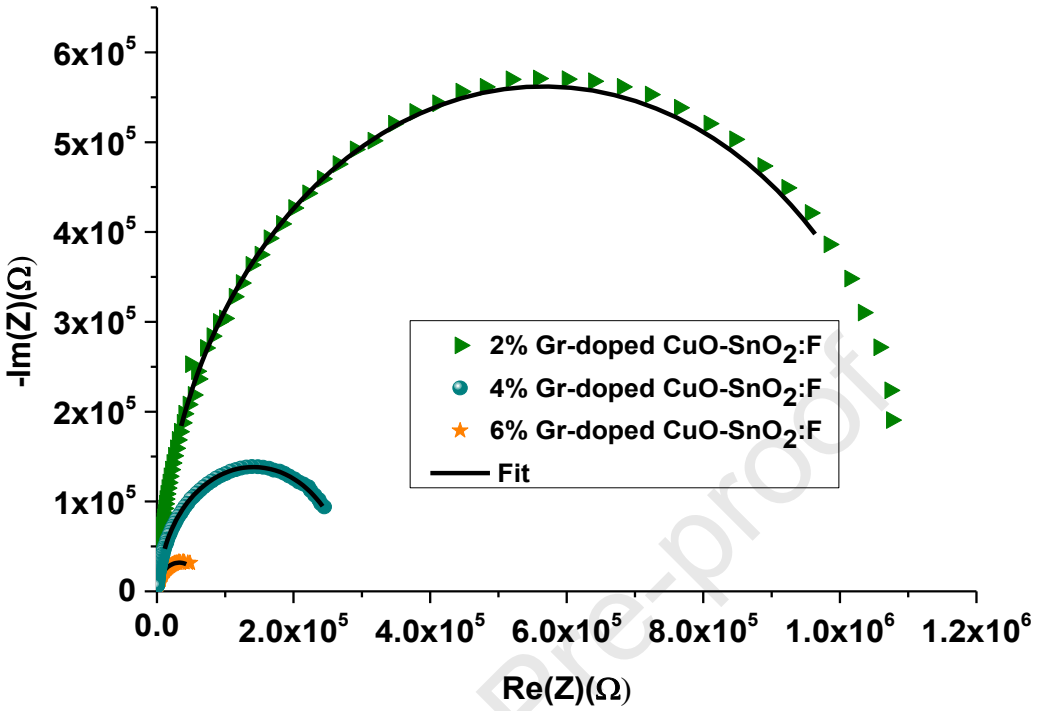




**Figure 9**

**(a)**

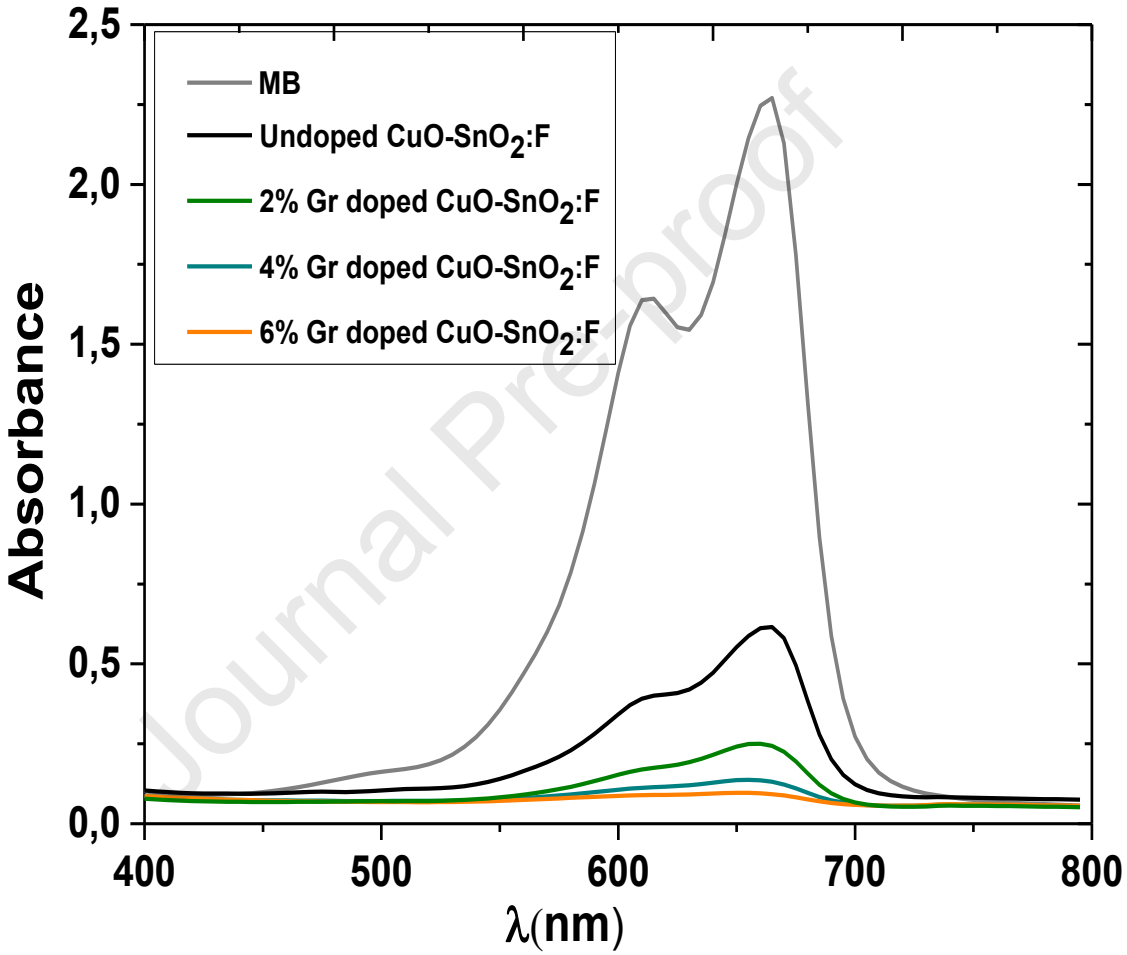

**(b)**

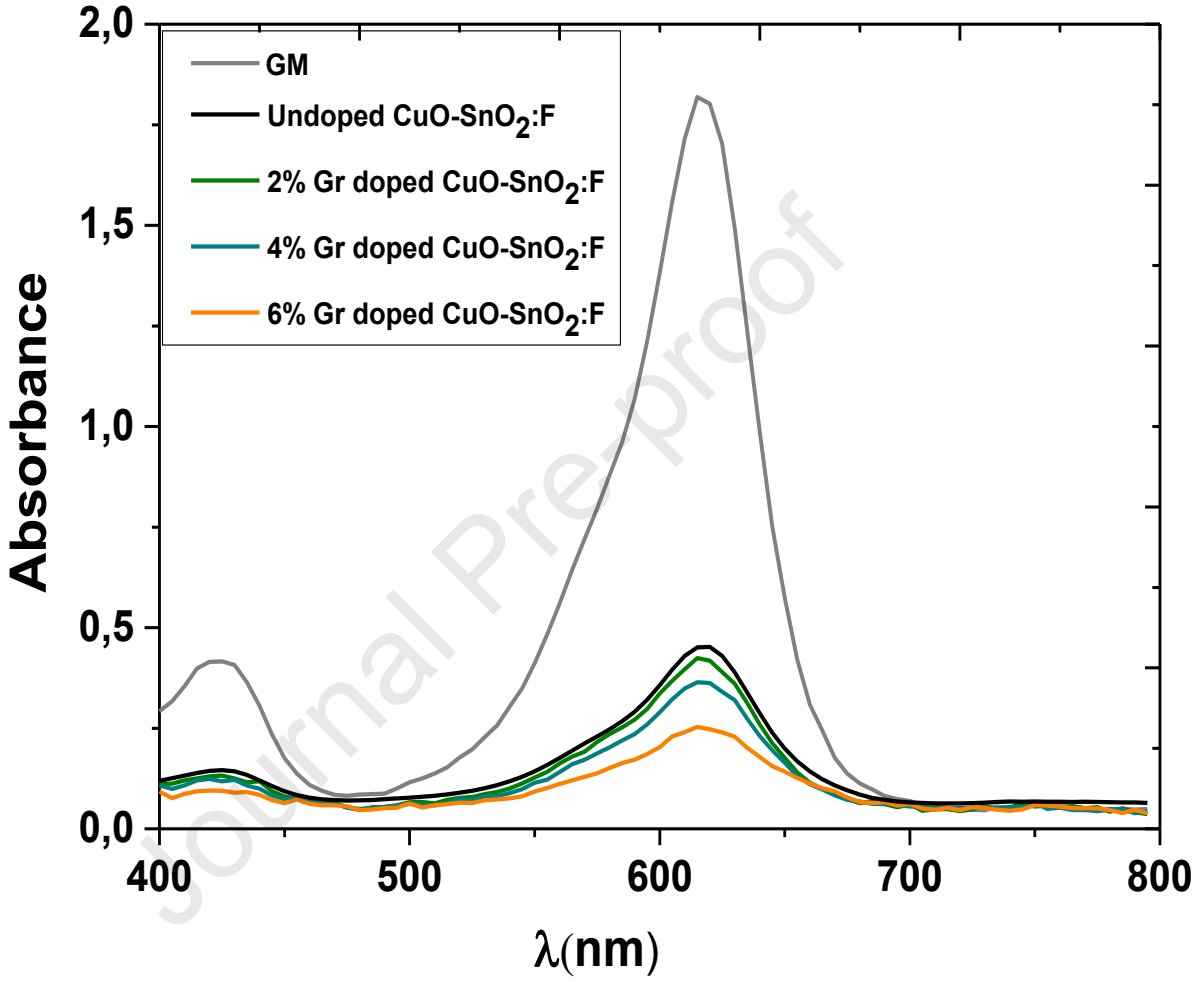

(c)

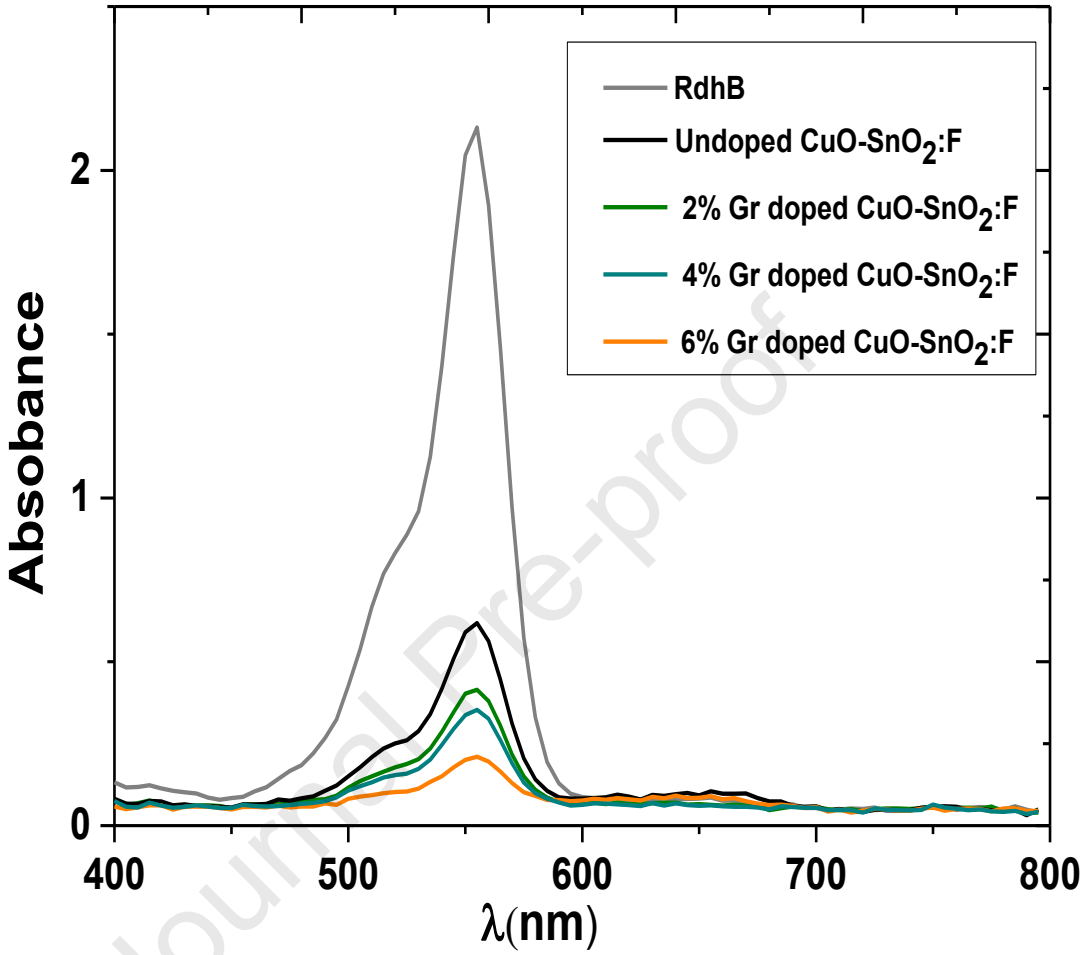

**Figure 10**

**(a)**

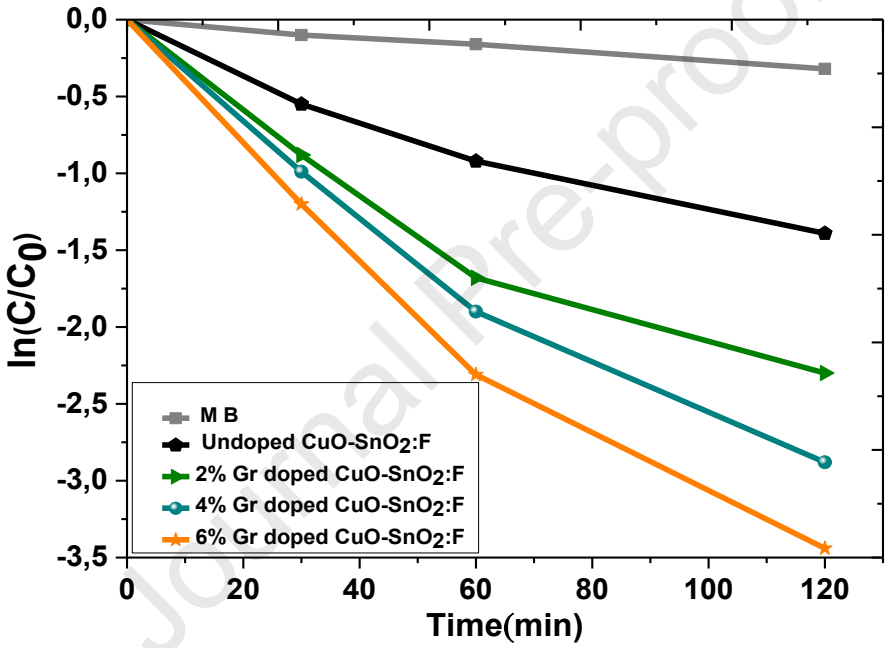




**(b)**

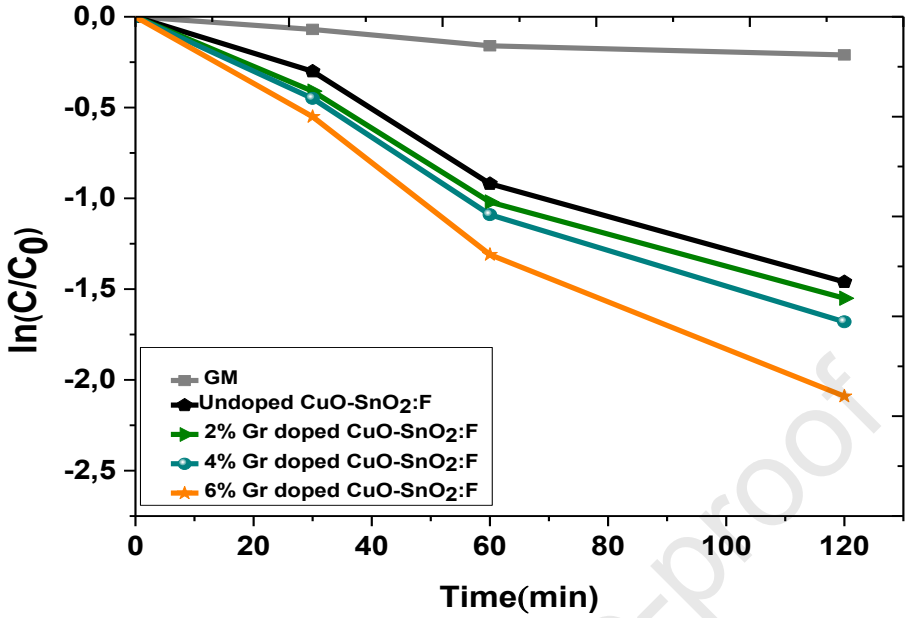




**(c)**

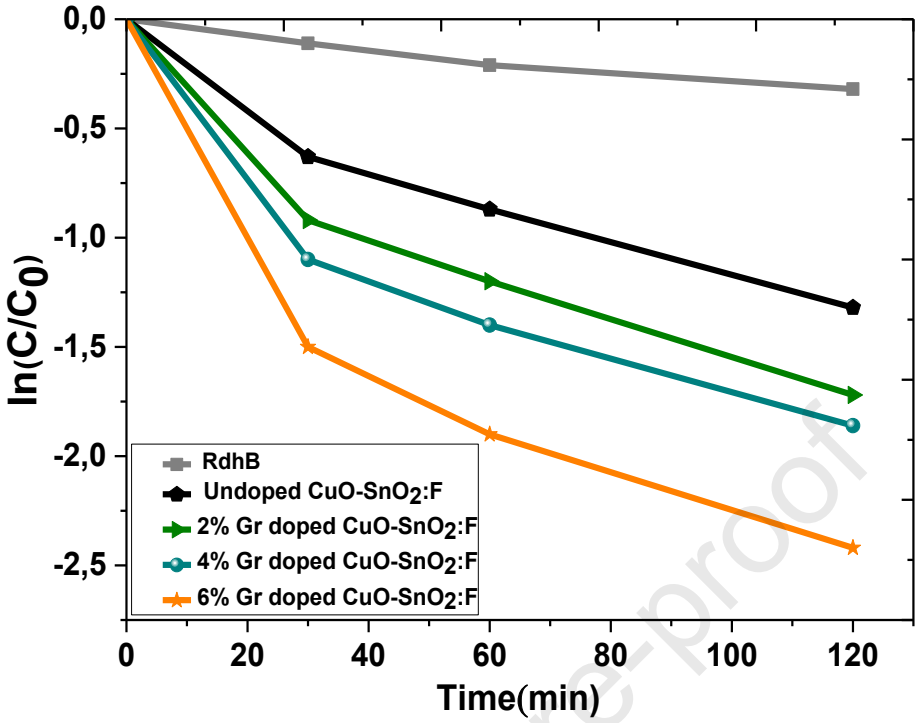

**Figure 11**

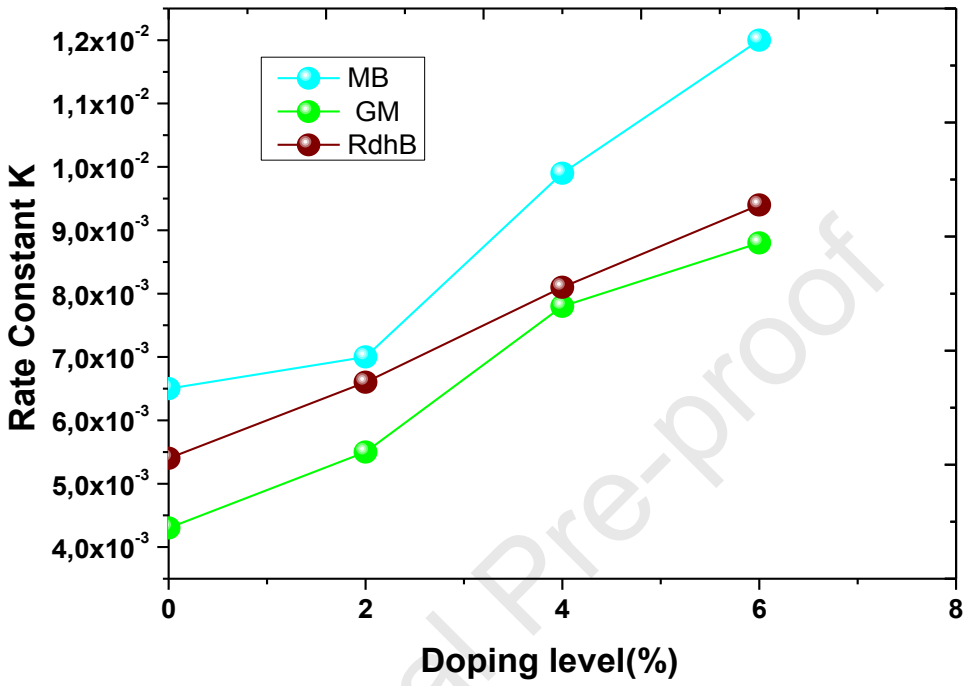

**Figure 12**

**(a)**

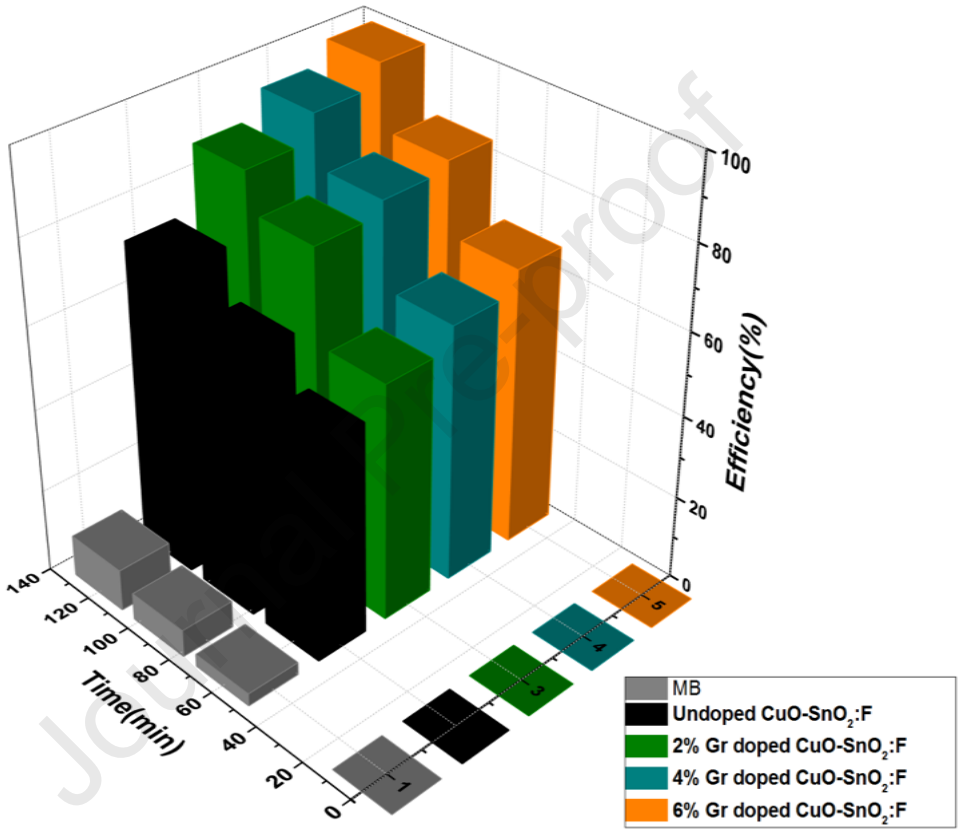
Efficiency(%)
100
80
60
40
20
0
Time(min)
140
120
100
80
60
40
20
0
1
2
3
4
5
MB
Undoped CuO-SnO2:F
2% Gr doped CuO-SnO2:F
4% Gr doped CuO-SnO2:F
6% Gr doped CuO-SnO2:F

**(b)**

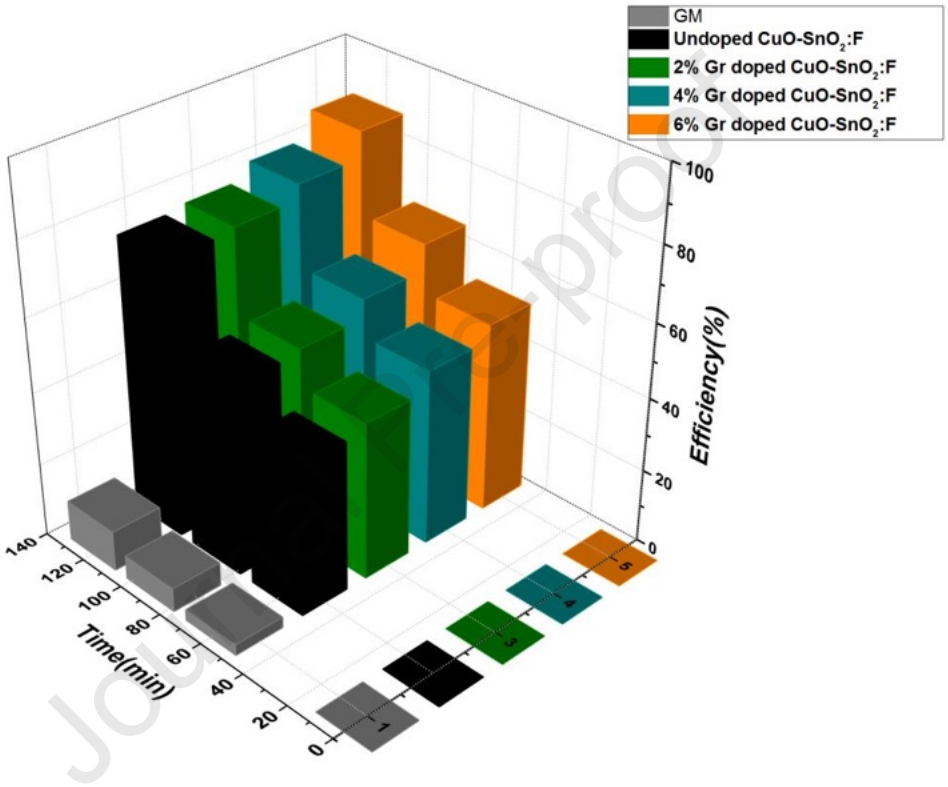

**(c)**

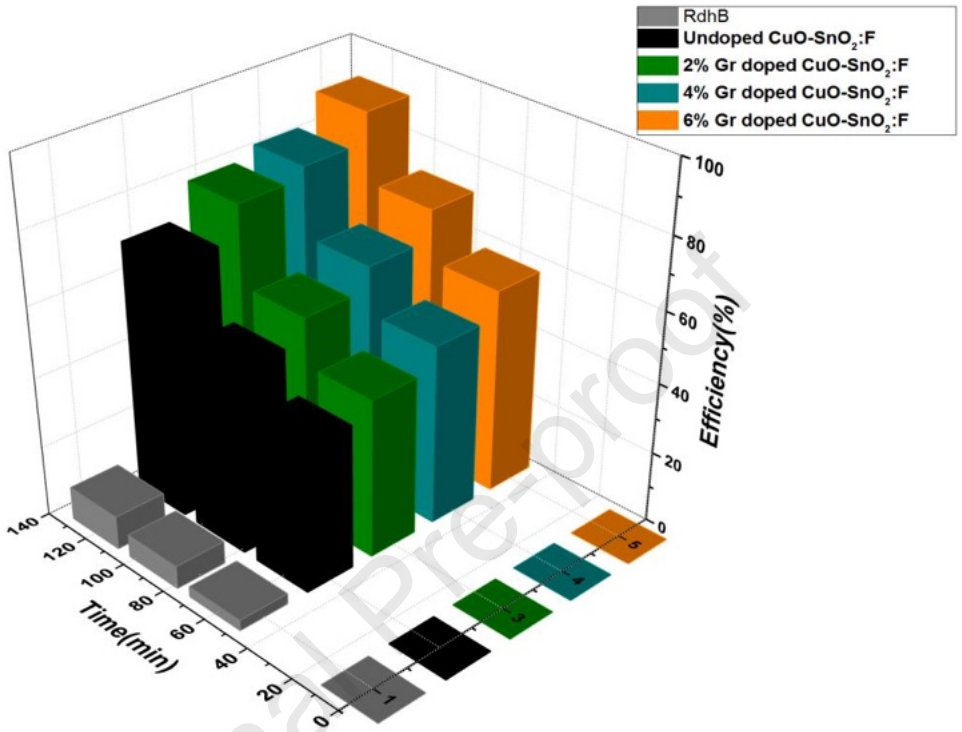

**Figure 13**

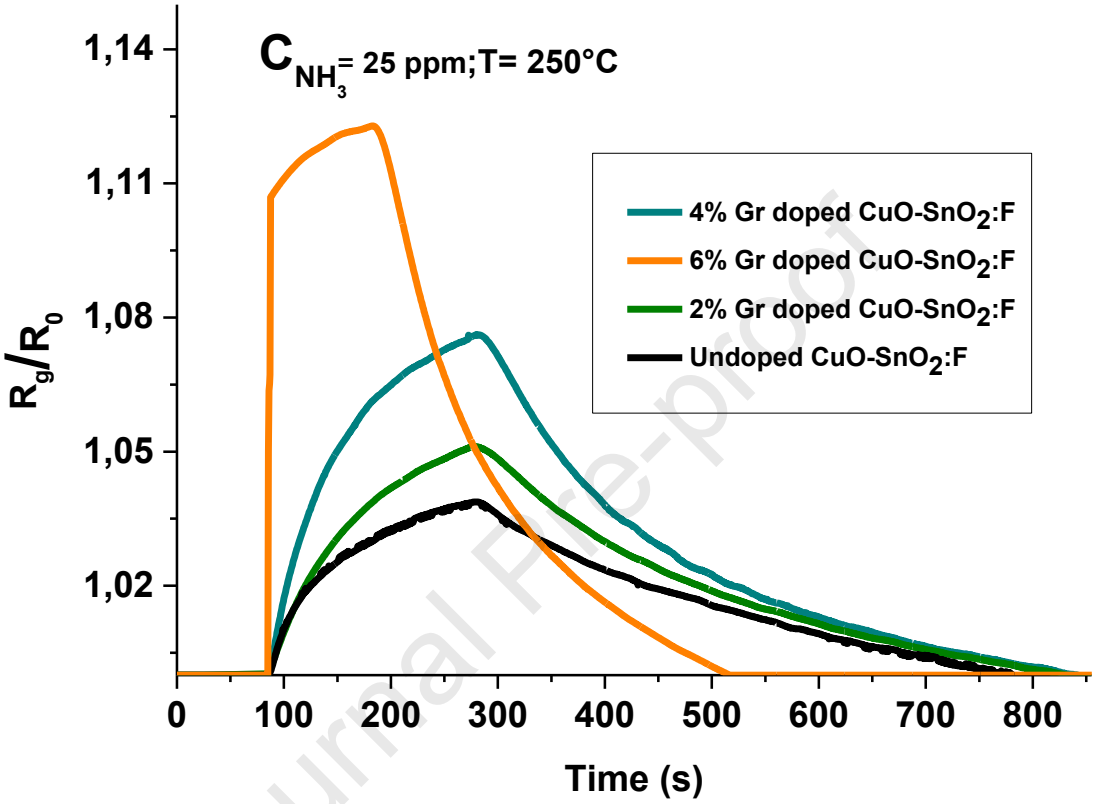

**Figure 14**

**(a)**

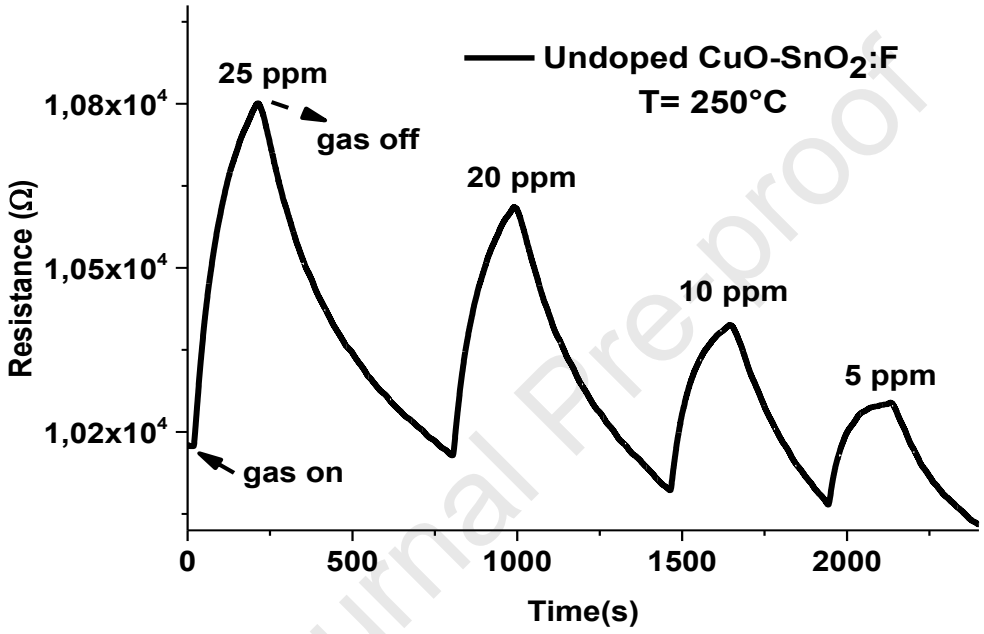


**(b)**

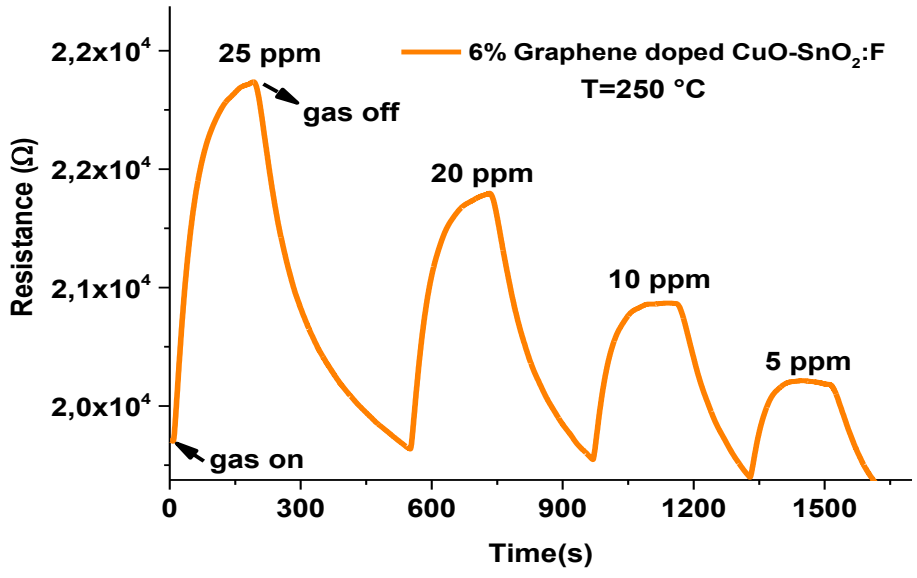

**Figure 15**

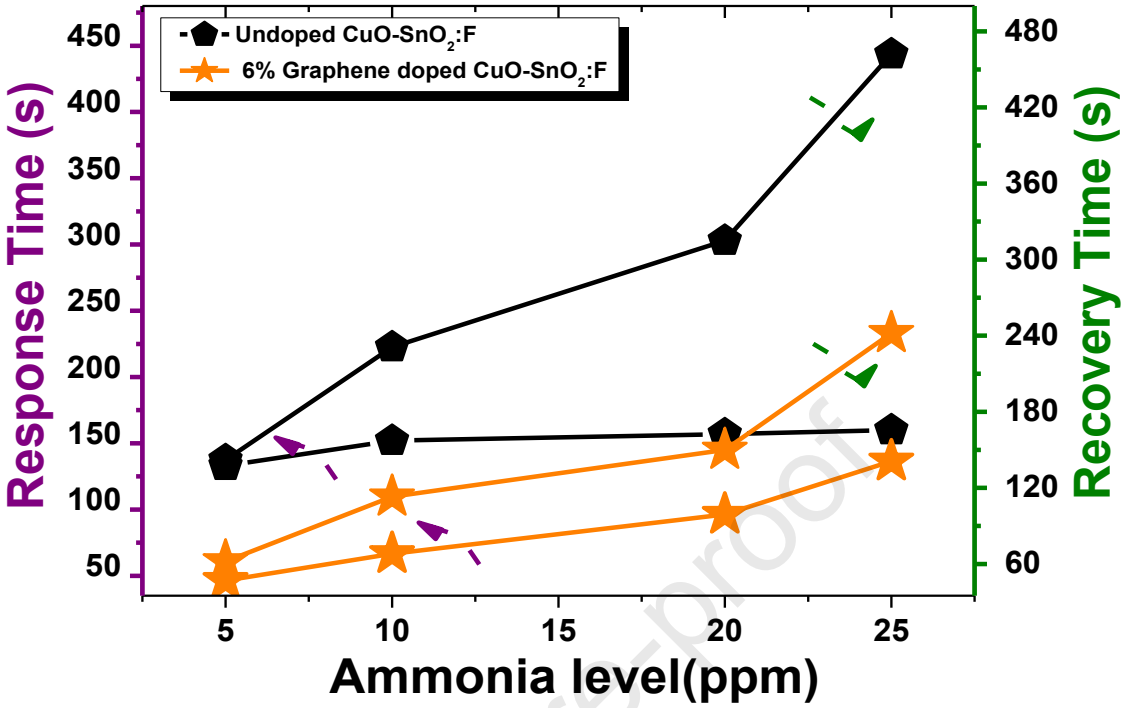

**Declaration of interest Statement**

The authors declare that they have no known competing financial interests or personal relationships that could have appeared to influence the work reported in this paper.